Visibility-derived aerosol optical depth over global land from 1980 to 2021

Hongfei Hao[1], Kaicun Wang[2], Chuanfeng Zhao[3], Guocan Wu[1], Jing Li[3]

[1]Global Change and Earth System Science, Faculty of Geographical Science, Beijing Normal University, Beijing 100875, China

[2]Institute of Carbon Neutrality, Sino French Institute of Earth System Science, College Urban and Environmental Sciences, Peking University, Beijing 100871, China

[3]Institute of Carbon Neutrality, Department of Atmospheric and Oceanic Sciences, School of Physics, College Urban and Environmental Sciences, Peking University, Beijing 100871, China

Corresponding Author: Email: kcwang@pku.edu.cn

Abstract

Long-term and high spatial resolution aerosol optical depth (AOD) data are essential for climate change detection and attribution. Global ground-based AOD observation stations are sparsely distributed, and satellite AOD observations have a low temporal frequency, as well low accuracy before 2000 over land. In this study, AOD is derived from hourly visibility observations collected at more than 5000 meteorological stations over global land from 1980 to 2021. The AOD retrievals of the Moderate Resolution Imaging Spectroradiometer (MODIS) onboard the Aqua Earth observation satellite are used to train the machine learning model, and the ERA5 reanalysis boundary layer height is used to convert the surface visibility to AOD. Comparisons with independent dataset show that the predicted AOD has correlation coefficients of 0.54 and 0.55 with Terra MODIS satellite retrievals and AERONET ground observations at daily time scale. The correlation coefficients are higher at monthly and annual scales, which are 0.81 and 0.61 for the monthly and 0.91 and 0.65 for the annual, compared with Terra MODIS and AERONET AOD, respectively. The visibility-derived AOD at station scale is gridded into a 0.5° grid by ordinary kriging interpolation. The mean visibility-derived AOD over the global land (-60°N-85°N), the Northern Hemisphere, and the Southern Hemisphere are 0.161, 0.158, and 0.173, with a trend of -0.0026/10a, -0.0018/10a, and -0.0059/10a from 1980 to 2021. For the regional scale, the mean (trend) of AOD are 0.145 (-0.0041/10a), 0.139 (-0.0021/10a), 0.131 (-0.0009/10a), 0.153 (-0.0021/10a), 0.192 (-0.0100/10a), 0.275 (-0.0008/10a), 0.177 (-0.0096/10a), 0.127 (-0.0081/10a), 0.177 (-0.0003/10a), 0.222 (-0.0000/10a), 0.232 (0.0071/10a), and 0.255 (0.0096/10a) in Eastern Europe, Western Europe, Western North America, Eastern North America, Central South America, Western Africa, Southern Africa, Australia, Southeast Asia, Northeast Asia, Eastern China, and India. The visibility-derived AOD at station and grid scales over global land from 1980 to 2021 are available at National Tibetan Plateau / Third Pole Environment Data Center (https://doi.org/10.11888/Atmos.tpdc.300822) (Hao et al., 2023).

How to cite. Hao, H., Wang, K., C. Zhao, Wu, G., J. Li (2023). Visibility-derived aerosol optical depth over global land (1980-2021). National Tibetan Plateau / Third Pole Environment Data

38   Center. https://doi.org/10.11888/Atmos.tpdc.300822.

1 Introduction

40   Atmospheric aerosols are composed of solid and liquid particles suspended in the atmosphere.
41   Aerosol particles are directly emitted into the atmosphere or formed through gas-particle
42   transformation (Calvo et al., 2013), with diverse shapes and sizes (Fan et al., 2021), optical
43   properties, and various components (Liao et al., 2015; Zhang et al., 2020; Li et al., 2022). Most
44   atmospheric aerosols are concentrated in the troposphere, especially in the boundary layer (Liu et
45   al., 2022), with a high concentration near emission sources (Kulmala et al., 2004) , and a small
46   portion are distributed in the stratosphere. Atmospheric aerosols severely impact the atmospheric
47   environment and human health. They deteriorate air quality, reduce visibility, and cause other
48   environmental issues (Wang et al., 2012; Boers et al., 2015). They impair human health or other
49   organisms' conditions by increasing cardiovascular and respiratory disease incidence and mortality
50   rates (Chafe et al., 2014; Yang et al., 2022). The Global Burden of Disease shows that global
51   exposure to ambient $PM_{2.5}$ resulted in 0.37 million deaths and 9.9 million disability-adjusted life
52   years (Chafe et al., 2014).

53   Aerosols are inextricably linked to climate change. Atmospheric aerosols alter the Earth's energy
54   budget and then affect the climate (Li et al., 2022). They cool the surface and heat the atmosphere
55   by scattering and absorbing solar radiation (Forster et al., 2007; Chen et al., 2022). Aerosols, such
56   as black carbon and brown carbon, also absorb solar radiation (Bergstrom et al., 2007), heat the
57   local atmosphere and suppress or invigorate convective activities (Ramanathan et al., 2001; Sun and
58   Zhao, 2020). Aerosols also alter the optical properties and life span of clouds (Albrecht, 1989).
59   Atmospheric aerosols strongly affect regional and global short-term and long-term climates through
60   direct and indirect effects (Mcneill, 2017).

61   Tropospheric aerosols are considered as the second largest forcing factor for global climate change
62   (Li et al., 2022), and they reduce the warming due to greenhouse gases by -0.5℃ (Ipcc, 2021).
63   However, aerosols are also regarded as the largest contributor to quantifying the uncertainty of
64   present-day climate change (Ipcc, 2021). The uncertainties are caused by the deficiencies of the
65   global descriptions of aerosol optical properties (such as scattering and absorption) and
66   microphysical properties (such as size and component), and the impact on cloud and precipitation,
67   further affecting the estimation of aerosol radiative forcing (Lee et al., 2016; Ipcc, 2021). Therefore,
68   sufficient aerosol observations are crucial. In aerosol measurements, aerosol optical depth (AOD)
69   is often used to describe its column properties, which represents the vertical integration of aerosol
70   extinction coefficients. AOD is an important physical quantity for estimating the content,
71   atmospheric pollution and climatology of aerosols (Zhang et al., 2020).

72   AOD data usually from ground-based and satellite-borne remote sensing observation. They have
73   both advantages and disadvantages. Ground-based lidar observation is an active remote sensing
74   technology. Lidar generally emits laser and receives backscattered signals to invert the extinction
75   coefficient of aerosols at different heights (Klett, 1985). By using the depolarization ratio, the type
76   of aerosol, such as fine particles or dust, can be distinguished (Bescond et al., 2013). The AOD
77   within a certain height can be calculated by integrating the extinction coefficients; however,
78   scattering signals are usually not received near the ground, leading to blind spots (Singh et al., 2019).

79 At present, there are many ground-based lidar worldwide and regional networks, which provides
80 important support of vertical changes in aerosols, such as the NASA Micro-Pulse Lidar Network
81 (MPLNET) in the early 1990s (Welton et al., 2002), the European Aerosol Research Lidar Network
82 (EARLINET) since 2000 (Bösenberg and Matthias, 2003), the Latin American Lidar Network
83 (LALINET) since 2013 (Guerrero-Rascado et al., 2016).

84 Ground-based remote sensing observations supply aerosol loading data (such as AOD), by
85 measuring the attenuation of radiation from the top of the atmosphere to the surface (Holben et al.,
86 1998). This type of observations mainly uses weather-resistant automatic sun and sky scanning
87 spectral radiometers to retrieve optical and microphysical aerosol properties (Che et al., 2014). The
88 Aerosol Robotic Network (AERONET) is a popular global network composed of NASA and
89 multiple international partners that provides high-quality and high-frequency aerosol optical and
90 microphysical properties under various geographical and environmental conditions (Holben et al.,
91 1998; Dubovik et al., 2000). The AERONET observations are extensively used to validate satellite
92 remote sensing observations and model simulations, as well as climatology study (Dubovik et al.,
93 2002b). There are many regional networks of sun photometers, such as the Maritime Aerosol
94 Network (MAN), which use a handheld sun photometer to collect data over the ocean and is merged
95 into AERONET (Smirnov et al., 2009), the China Aerosol Robot Sun Photometer Network
96 (CARSNET) (Che et al., 2009), the Canadian sub-network of AERONET (AEROCAN) (Bokoye et
97 al., 2001), Aerosol characterization via Sun photometry: Australian Network (AeroSpan)
98 (Mukkavilli et al., 2019), and the sky radiometer network (SKYNET) in Asia and Europe (Kim et
99 al., 2004; Nakajima et al., 2020). Another very valuable global network is the NOAA/ESRL
100 Federated Aerosol Network (FAN), which uses integrated nephelometers distinct from sun
101 photometers, mainly located in remote areas, providing background aerosol properties over 30 sites
102 (Andrews et al., 2019).

103 Satellite remote-sensing is a space-based method that can provide aerosol properties worldwide.
104 With the development of satellite remote sensing technology since 1970s, aerosol distributions can
105 be extracted with the advantage of sufficient real-time and global coverage from multiple satellite
106 sensors (Kaufman and Boucher, 2002; Anderson et al., 2005). The Advanced Very High Resolution
107 Radiometer (AVHRR) is the earliest sensor used for retrieving AOD over ocean (Nagaraja Rao et
108 al., 1989). The Moderate Resolution Imaging Spectroradiometer (MODIS), on board the Terra
109 (launched in 1999) and Aqua (launched in 2002) satellites is a popular sensor with 36 channels,
110 which have been used for AOD retrieval over both ocean and land based on the Dark Target and the
111 Deep Blue algorithms (Remer et al., 2005; Levy et al., 2013). The latest MODIS AOD data version
112 is the Collection 6.1, which provides global AOD over 20 years (Wei et al., 2019). There are also
113 many other satellite sensors that can be used to retrieve AOD, such as the Polarization and
114 Directionality of the Earth's Reflectances (POLDER) during 1996-1997, 2003 and 2004-2013
115 (Deuzé et al., 2000), Sea-viewing Wide Field-of-view Sensor (SeaWIFS) during 1997-2007
116 (O'reilly et al., 1998), the Multi-angle Imaging Spectroradiometer (MISR) on Terra since 1999
117 (Diner et al., 1998). The Cloud-Aerosol Lidar with Orthogonal Polarization (CALIOP) has also
118 derived aerosols in the vertical direction since 2006 (Winker et al., 2009).

119 These measurements provide important data for studying the global and regional spatiotemporal
120 variabilities and climate effect of aerosols. However, ground-based remote sensing observations
121 only provide aerosol properties with low spatial coverage. There were only 1126 ground stations

122 worldwide in 2002 and even fewer sites were available for climate analysis (Holben et al., 1998;
123 Chu et al., 2002), which limited aerosol climate research by spatial coverage (Bright and Gueymard,
124 2019). Satellite remote sensing overcomes the limitations of spatial coverage. The AVHRR has been
125 used to retrieve AOD since 1980, but it is limited by a few channel number, low spatial resolution,
126 and insufficient validation through ground-based observations before 2000 (Hsu et al., 2017). Many
127 studies have only investigated the trends and distributions of aerosols after 2000 (Bösenberg and
128 Matthias, 2003; Winker et al., 2013; Xia et al., 2016; Tian et al., 2023), because of the lack of long-
129 term and global cover AOD products, which is the bottleneck for aerosol climate change detection
130 and attributions.

131 To overcome these limitations and enrich aerosol data, alternative observation data could be utilized
132 to derive AOD. Atmospheric horizontal visibility is a suitable alternative (Wang et al., 2009; Zhang
133 et al., 2020), because it has the advantages of the long-term records with a large number of stations
134 worldwide.

135 Atmospheric visibility is a physical quantity that describes the transparency of the atmosphere
136 through manual and automatic observations, and the automatic observations of visibility usually
137 measure atmospheric extinction (scattering coefficient and transmissivity). Koschmieder (1924)
138 first proposed the relationship between the meteorological optical range and the total optical depth.
139 Elterman (1970) futher established a formula between AOD and visibility by assuming an
140 exponential decrease in aerosol concentration with altitude, considering the extinction of molecules
141 and ozone to analyze air pollution, which called the Elterman model. Qiu and Lin (2001) corrected
142 the Elterman model by considering the influence of water vapor and used two water vapor pressure
143 correction coefficients to retrieve AOD of 16 stations in China in 1990. Wang et al. (2009) analyzed
144 the trend of AOD using visibility-based retrivals from 1973 to 2007 over land. Lin et al. (2014)
145 retrieved the AOD in eastern China in 2006 using visibility and aerosol vertical profiles provided
146 by GEOS-Chem. Wu et al. (2014) and Zhang et al. (2017) parameterized the constants in the
147 Elterman model and use satellite retrieved AOD to solve the parameters in the models at different
148 stations, to retrive the long-term AOD in China.

149 Zhang et al. (2020) reviewed the methods of visibility retrieval of AOD, indicating that visibility-
150 based retrieval of AOD can compensate for the shortcomings of long-term aerosol observation data.
151 Simultaneously, various parameters, such as station altitude, consistency of visibility data, water
152 vapor and aerosol vertical profiles (scale height), were discussed with modified suggestions
153 proposed. These studies have enriched AOD data regionally. These studies have enriched aerosol
154 data insome extent. At present, there are very few studies on global visibility-retrieved AOD and to
155 analyze climatology of aerosols.

156 The two physical quantities of visibility and AOD have both connections and differences, making it
157 challenging to retrieve AOD from visibility. Visibility represents the maximum horizontal visible
158 distance near the surface, while AOD represents the total vertical attenuation of solar radiation by
159 aerosols. The visibility of automatic observation is dependent on the local horizontal atmosphereic
160 extinction (Noaa et al., 1998). Visibility has not a simple linear relationship with meteorological
161 factors. The vertical structure of aerosols is the greatest challenge to obtain, as it is not a simple
162 hypothetical curve in complex terrain and circulation conditions (Zhang et al., 2020). These
163 limitations make it more complex to derive AOD. Machine learning methods can effectively address

complex nonlinear relationships between variables and have been widely applied in remote sensing and climate research fields. Li et al. (2021) used the random forest method to predict $PM_{2.5}$ in Iraq and Kuwait based on satellite AOD during 2001-2018. Kang et al. (2022) applied LightGBM and random forest to estimate AOD over East Asia, and the results showed a consistency with AERONET. Dong et al. (2023) derived aerosol single scattering albedo from visibility and satellite AOD over 1000 global stations. Hu et al. (2019) used a deep learning method to retrieve horizontal visibility from MODIS AOD. These studies have confirmed the ability of machine learning to effectively solve complex relationships among variables. And previous studies are mostly conducted at the regional or national scale, and few studies at the global scale. Thus, it is feasible to derive AOD from atmospheric visibility over global land by using the machine learning method.

In this study, we propose a machine learning method to derive AOD, where satellite AOD is the target value, and visibility and other related meteorological variables are the predictors. We explain the robustness of the model, validate the model's predictions using ground-based AOD and independent satellite retrievals, and analyze the mean and trend of AOD across land and regions. Two datasets of long-term high-resolution AOD are generated. The Section 2 introduces the data and method. The Section 3 is the evaluation and validation of the visibility-derived AOD, and the distribution and trends are discussed at global and regional scales. The Section 4 presents the conclusions. This study is dedicated to supporting the research of aerosols in climate change detection and attribution.

2 Data and method

2.1 Study area

The study area is global land. A total of 5032 meteorological stations and 395 AERONET sites are selected in this study, shown in Figure 1. Twelve regions are selected for special analysis, including Eastern Europe, Western Europe, Western North America, Eastern North America, Central South America, Western Africa, Southern Africa, Australia, Southeast Asia, Northeast Asia, Eastern China, and India. The time range of the study is from 1980 to 2021, during which the records of meteorological stations are sufficient with a uniform spatial distribution. As shown in Figure 1, the daily records have exceeded 1500 stations, and monthly and annual records have exceeded 2000 during 1980-1990. After 2000, monthly records have reached 3000, which is the foundation of gridding AOD.

194
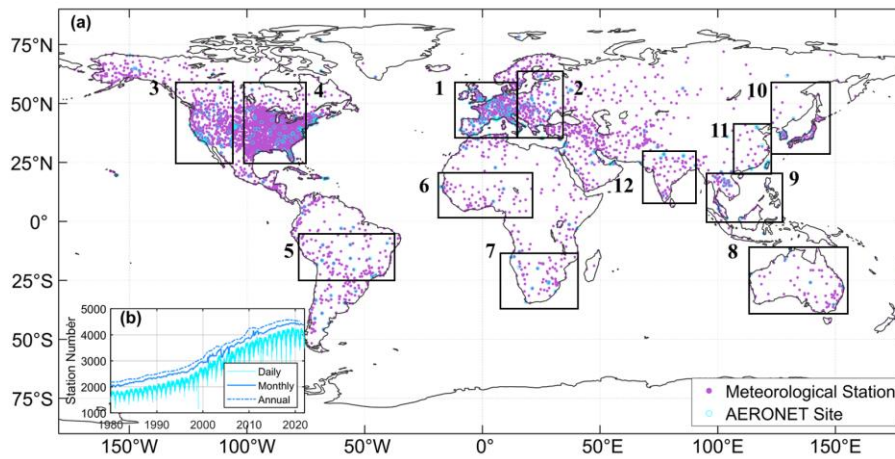
Figure 1 Study area (a) and the meteorological station number (b) with daily, monthly, and annual records. The number of meteorological stations (filled circles) is 5032. The number of AERONET sites (empty circles) is 395. The box regions of labelled with number 1-12 are Eastern Europe, Western Europe, Western North America, Eastern North America, Central South America, Western Africa, Southern Africa, Australia, Southeast Asia, Northeast Asia, Eastern China, and India.

2.2 Meteorological data

The ground hourly data from 1980 to 2021 is collected from 5032 automated meteorological stations of airports over land. Automated surface observations reduce errors associated with human involvement in data collection, processing, and transmission. The data can be downloaded at https://mesonet.agron.iastate.edu/ASOS. The data is extracted from the Meteorological Terminal Aviation Routine Weather Report (METAR). The World Meteorological Organization (WMO) sets guidelines for METAR reports, including report format, encoding, observation instruments and methods used, data accuracy, and consistency. These requirements ensure consistency and comparability of METAR reports globally. International regulations can be referenced at https://community.wmo.int/en/implementation-areas-aeronautical-meteorology-programme. Among them, over 1,000 stations belong to the Automated Surface Observing System (ASOS), and others are sourced from airport reports around the world.

The daily average visibility is calculated using harmonic mean. Experiments have found that harmonic average visibility can better detect the weather phenomena than arithmetic average visibility (Noaa et al., 1998). The visibility is calculated using the extinction coefficient, which is directly proportional to the reciprocal of visibility (Wang et al., 2009). Harmonious average visibility can capture the process of visibility decline more quickly. Therefore, daily visibility will have greater representativeness:

$$V = n/(\frac{1}{V_1} + \frac{1}{V_2} + \cdots + \frac{1}{V_n}) \qquad \textbf{Eq. 1}$$

where V is the harmonic mean visibility, n = 24 for the daily visibility, and V_1, V_2,... V_n are the individual hourly visibility.

In addition to hourly visibility (VIS), other variables closely related to aerosol properties are selected,

including relative humidity (RH), dew point temperature (DT), temperature (TMP), wind speed (WS) and sea-level pressure (SLP). Temperature affects atmospheric stability and the rate of secondary particle formation, and humidity influences the size and hygroscopic growth, and wind speed and pressure significantly impact the transport and deposition. Sky conditions (cloud amount) and hourly precipitation are also selected to remove the records of extensive cloud cover and precipitation.

We processed the data as follows. The records with missing values are eliminated (Husar et al., 2000). When over 80% overcast or fog, the records of sky conditions are eliminated, though such situations occur less than 1% of the time over land (Remer et al., 2008). The records with 1-hour precipitation greater than 0.1 mm are eliminated. We calculate the temperature dew point difference (dT). When the RH is greater than 90%, it is impossible to distinguish whether it is fog or haze, or both, and even precipitation. The records with RH greater than or equal to 90% are eliminated. When the RH is less than 30%, the dilution effect of aerosols is very low or even negligible. When RH is between 30% and 90%, visibility is converted to dry visibility (Yang et al., 2021c):

$$VISD = VIS/(0.26 + 0.4285 * log(100 - RH)) \qquad \textbf{Eq. 2}$$

where VISD is the dry visibility.

Daily average of variables are calculated by at least 3 hourly records.

2.3 Boundary layer height

The hourly boundary layer height (BLH) from 1980 to 2021 is available from the Fifth Generation reanalysis of the European Medium-Range Weather Forecast Center (ERA5) with a resolution of 0.25° x 0.25° (https://cds.climate.copernicus.eu), which is the successor of ERA-Interim and has undergone various improvements (Hersbach et al., 2020). The atmospheric boundary layer is the layer closest to the Earth's surface and exhibits complex turbulence activities, and its height undergoes significant diurnal variation. The effects of the boundary layer on aerosols are mainly manifested in vertical distribution, concentration changes, transport, and deposition (Ackerman et al., 1995). The characteristics and variations in the boundary layer play a crucial role in regulating and adjusting the distribution of atmospheric aerosols. The boundary layer height serves as an approximate measure of the scale height for aerosols (Zhang et al., 2020).

Compared to observations of 300 stations over world from 2012 to 2019, the BLH of ERA5 was underestimated by 131.96m. Compared with the underestimated MERRA-2 (166.35m), JRA-55 (351.49m), and NECP-2 (420.86m), the BLH of ERA5 was closest to the observations (Guo et al., 2021). The BLH hourly data is temporally and spatially matched with the meteorological data before calculating the daily average.

Because the inverse of visibility is proportional to the extinction coefficient and positively related to AOD (Wang et al., 2009), we calculated the reciprocal of visibility (VISI) and the reciprocal of dry visibility (VISDI). Due to the influence of boundary layer height on the vertical distribution of particles (Zhang et al., 2020), we calculated the product (VISDIB) of the reciprocal of dry visibility and BLH. Therefore, the Predictor (Figure 2) is composed of 11 variables (TMP, Td, dT, RH, SLP, WS, VIS, BLH, VISI, VISDI, and VISDIB).

2.4 MODIS AOD Products

Satellite daily AOD is available from the Moderate Resolution Imaging Spectroradiometer (MODIS) Level 3 Collection 6.1 AOD products of the Aqua (MYD09CMA) satellite from 2002 to 2021 and Terra (MOD09CMA) satellite from 2000 to 2021 with a spatial resolution of 0.05° x 0.05° at a wavelength of 550 nm (https://ladsweb.modaps.eosdis.nasa.gov). MOD/MYD09 has a higher spatial resolution than MOD/MYD08 (1° x 1°), which may result in a greater difference in AOD values and reduce the proximity ratio to match the visibility-derived AOD at station scale. Terra (passing approximately 10:30 am local time) and Aqua (passing approximately 1:30 pm local time) were successfully launched in December 1999 and May 2002, respectively.

MODIS, carried on the Terra and Aqua satellites is a crucial instrument in the NASA Earth Observing System program, which is designed to observe global biophysical processes (Salomonson et al., 1987). The 2,330 km-wide swath of the orbit scan can cover the entire globe every one to two days. MODIS has 36 channels and more spectral channels than previous satellite sensors (such as AVHRR). The spectral range from 0.41 to 15μm representing three spatial resolutions: 250 m (2 channels), 500 m (5 channels), and 1 km (29 channels). The aerosol retrieval algorithms use seven of these channels (0.47–2.13μm) to retrieve aerosol characteristics and uses additional wavelengths in other parts of the spectrum to identify clouds and river sediments. Therefore, it has the ability to characterize the spatial and temporal characteristics of the global aerosol field.

The MODIS aerosol product actually takes use of different algorithms for deriving aerosols over land and ocean. The Dark Target (DT) algorithm is applied to densely vegetated areas because the surface reflectance over dark-target areas was lower in the visible channels and had nearly fixed ratios with the surface reflectance in the shortwave and infrared channels (Levy et al., 2007; Levy et al., 2013). The Deep Blue (DB) algorithm was originally applied to bright land surfaces (such as deserts), and later extended to cover all cloud-free and snow-free land surfaces (Hsu et al., 2006; Hsu et al., 2013). MODIS Collection 6.1 aerosol product was released in 2017, incorporating significant improvements in radiometric calibration and aerosol retrieval algorithms.

The expected errors are $\pm (0.05 \pm 15\%)$ for the DT retrievals over land. Higher spatial coverage is observed in August and September, reaching 86-88%. During December and January, due to the presence of permanent ice and snow cover in high-latitude regions of the Northern Hemisphere, the spatial coverage is 78-80%. Thus, challenges remain in retrieving AOD values in high-latitude regions (Wei et al., 2019). However, visibility observations are available in high-latitude regions, thereby partially addressing the lack in these regions.

In this study, the Terra and Aqua MODIS AOD are temporally and spatially matched with the meteorological stations. Aqua MODIS AOD is used as the Target, when training the model, and Terra MODIS AOD is used in the evaluation and validation of the model results, as shown in the flowchart (Figure 2).

2.5 Ground-based AOD

Ground-based 15-minute AOD data are available from the Aerosol Robotic Network (AERONET) Version 3.0 Level 2.0 product at 395 stations (Figure 1), which can be downloaded from https://aeronet.gsfc.nasa.gov. The AERONET program is a federation of ground-based remote sensing aerosol networks established by NASA and PHOTONS, including many subnetworks (such as AeroSpan, AEROCAN, NEON, and CARSNET). The sun photometer (CE-318) measures spectral sun and sky irradiance in the 340-1020 nm spectral range. When the aerosol loading is low,

the error is significant. When the AOD at 440 nm wavelength is less than 0.2, the error is 0.01, which is equivalent to the error of the absorption band in the total optical depth (Dubovik et al., 2002a). The total uncertainty in AOD under cloud-free conditions is less than ±0.01 for wavelength more than 440 nm, and ±0.02 for wavelength less than 440 nm (Holben et al., 1998). AERONET has three levels of AOD products: Level 1.0 (unscreened), Level 1.5 (cloud screened), and Level 2.0 (cloud screened and quality assured). Compared to Version 2, the Version 3 Level 2.0 database has undergone further cloud screening and quality assurance, which is generated based on Level 1.5 data with pre- and post-calibration and temperature adjustment and is recommended for formal scientific research (Giles et al., 2019). AERONET provides AOD products at wavelengths of 440, 675, 870, and 1020 nm. The AOD at 440nm and the Ångström index at 440-675nm are used for AOD at 550 nm not provided by AERONET, as shown in Eq. 3. AERONET AOD, as the 'true' value, is the average of at least two times within 1 hour (± 30 minutes) of Aqua transit time (Wei et al., 2019).

$$\tau_{550} = \tau_{440}\left(\frac{550}{440}\right)^{-\alpha} \qquad \textbf{Eq. 3}$$

where τ_{440} and τ_{550} are the AOD at a wavelength of 440nm and 550 nm, and α is the Ångström index.

The matching conditions between AERONET sites and meteorological stations are (1) a distance of less than 0.5 ° (2) at least three years of observation. Finally, a total of 395 pairs were matched.

2.6 Decision Tree Regression

2.6.1 Feature selection

Although a multidimensional dataset can provide as much potential information as possible for AOD, irrelevant and redundant variables can also introduce significant noise in the model and reduce the model's accuracy and stability (Kang et al., 2021; Dong et al., 2023). Therefore, the F-test is used to search for the optimal feature subset in the Predictor, aiming to eliminate irrelevant or redundant features and select truly relevant features, which helps to simplify the model's input and improve the model's prediction ability (Dhanya et al., 2020). The F-test is a statistical test that gives an f-score(=-log(p), p represents the degree to which the null hypothesis is not rejected) by calculating the ratio of variances. In this study, we calculate the ratio of variance between the Predictors and Target, and the features are ranked based on higher values of the f-score. A greater value of f-score means that the distances between Predictors and Target are less and the relationship is closer, thus, the feature is more important. We set p=0.05. When the score is less than -log (0.05), the variable in the Predictors is not considered.

2.6.2 Data balance

When it is clear, the AOD value is small, the variability of AOD is small (AOD<0.5), and the data is concentrated near the mean value. When heavy pollution, the AOD value is large (AOD>0.5). Compared to clear sky, the AOD sequence will show "abnormal" large values with low frequency, which is the imbalance of AOD data.. When dealing with imbalanced datasets, because of the tendency of machine learning algorithms to perform better on the majority class and overlook the minority class, the model can be underfit (Chuang and Huang, 2023). Data augmentation techniques are commonly employed to

344 address the issue in imbalance data, which applies a series of transformations or expansions to generate
345 new training data, thereby increasing the diversity and quantity of the training data.

346 The Adaptive Synthetic Sampling (ADASYN) is a data augmentation technique specifically designed to
347 address data imbalance problem (He et al., 2008; Mitra et al., 2023). It is an extension of the Synthetic
348 Minority Over-sampling Technique (SMOTE) algorithm (Fernández et al., 2018). The goal of ADASYN
349 is to generate synthetic sample data for the minority class to increase its representation in the dataset.
350 ADASYN, which adaptively adjusts the generation ratio of synthetic samples based on the density
351 distribution of sample data, improves the dataset balance and enhances the performance of machine
352 learning models in dealing with imbalanced data.

353 The processing of imbalanced data includes (1) AOD sequences are classified into three types based on
354 percentile (0-1%, 2% -98%, 99%), (2) When the mean of the third type of AOD is greater than 5 times
355 the standard bias of the second type, it is considered an imbalanced sequence. These data, with a total
356 amount less than 5% of the sample, are imbalanced data, and (3) Then synthetic samples are generated
357 with the upper limit 10% of the samples.

358 **2.6.3 Decision Tree Regression Model**

359 The decision tree is a machine learning algorithm based on a tree-like structure used to solve
360 classification and regression problems. We adopt the CART algorithm to construct a regression tree by
361 analyzing the mapping relationship between object attributes (Predictors) and object values (Target). The
362 internal nodes have binary tree structures with feature values of "yes" and "no". In addition, each leaf
363 node represents a specific output for a feature space. The advantages of the regression tree include the
364 ability to handle continuous features and the ease of understanding the generated tree structure (Teixeira,
365 2004; Steinberg and Colla, 2009). Before training the tree model, the variables (Input) are normalized to
366 improve model performance, and after prediction, the results are obtained by denormalization. The 10-
367 fold cross-validation method is employed to improve the generalization ability of the model (Browne,
368 2000).

369 The core problems of the regression tree need to be solved are to find the optimal split variable and
370 optimal split point. The optimal split point of Predictors is determined by the minimum MSE, which in
371 turn determines the optimal tree structure. We set $Y = [y_1, y_2, ..., y_N]$ as the Target. We set $X = [x_1, x_2, ..., x_N]$ as the Predictors, $x_i = (x_i^1, x_i^2, ... x_i^n), i = 1,2,3 ..., N$, where n is the feature number, and
373 N is the length of sample. We set a training dataset as $D = [(x_1, y_1), (x_2, y_2), ..., (x_N, y_N)]$.

374 A regression tree corresponds to a split in the feature space and the output values on the split domains.
375 Assuming that the input space has been divided into M domains $[R_1, R_2, ..., R_M]$ and there is a fixed
376 output value on each R_M domain, the regression tree model can be represented as follows:

377
$$f(x) = \sum_{m=1}^{M} c_m I(x \in R_M), m = 1, 2, ..., M \qquad \textbf{Eq. 4}$$

378 where I is the indicator function (Eq. 5):

379
$$I = \begin{cases} 1, x \in R_m \\ 0, x \notin R_m \end{cases} \qquad \textbf{Eq. 5}$$

380 When the partition of the input space is determined, the square error can be used to represent the
381 prediction error of the regression tree for the training data, and the minimizing square error is used to

382 solve the optimal output value on each domain. The optimal value $(\widehat{c_m})$ on a domain is the mean of the
383 outputs corresponding to all input, namely:

$$\widehat{c_m} = ave(y_i | x_i \in R_m) \qquad \text{Eq. 6}$$

385 A heuristic method is used to split the feature space in CART. After each split, all values of all features
386 in the current set are examined individually, and the optimal one is selected as the split point based on
387 the principle of minimum sum of the square errors. The specific step is described as follows: for the
388 training dataset D, we recursively divide each region into two sub domains and calculate the output
389 values of each sub domain; then, construct a binary decision tree. For example, split variable is x^j and
390 split point is s. Then, in the domain $R_1(j,s) = [x | x^j \leq s]$ and domain $R_2(j,s) = [x | x^j > s]$, we can
391 solve the loss function $L(j,s)$ to find the optimal j and s.

$$L(j,s) = \sum_{x_i \in R_1(j,s)}(y_i - c_1)^2 + \sum_{x_i \in R_2(j,s)}(y_i - c_2)^2 \qquad \text{Eq. 7}$$

393 When $L(j,s)$ is the smallest, x^j is the optimal split variable and s is the optimal split point for the
394 x^j.

$$\min_{j,s}\left[\min_{c_1}\sum_{x_i \in R_1(j,s)}(y_i - c_1)^2 + \min_{c_2}\sum_{x_i \in R_2(j,s)}(y_i - c_2)^2\right] \qquad \text{Eq. 8}$$

396 We use the optimal split variable x^j and the optimal split point s to split the feature space and calculate
397 the corresponding output value.

$$\widehat{c_1} = ave(y_i | x_i \in R_1(j,s)), \ \widehat{c_2} = ave(y_i | x_i \in R_2(j,s)) \qquad \text{Eq. 9}$$

399 We traverse all input variables to find the optimal split variable x^j, forming a pair (j,s). Divide the
400 input space into two regions accordingly. Next, repeat the above process for each region until the stop
401 condition is met. The regression tree is generated.

402 Therefore, the regression tree model $f(x)$ can be represented as follows:

$$f(x) = \sum_{m=1}^{M}\widehat{c_m}I(x \in R_M), m = 1,2,...,M \qquad \text{Eq. 10}$$

404 **2.7 Gridding method**

405 Kriging is a regression algorithm to model and predict (interpolate) random processes/fields based on the
406 covariance function, which is widely used in geo-statistics (Pebesma, 2004). Ordinary Kriging is the
407 earliest and most extensively studied form of Kriging. It is a linear estimation system applicable to any
408 intrinsic stationary random field that satisfies the assumption of isotropy. The two key parameters of
409 Ordinary Kriging are the semi-variogram function and the weight factors (Goovaerts, 2000). It has been
410 widely applied in fields, such as climatology, environmental science, and agriculture (Lapen and Hayhoe,
411 2003; Chen et al., 2010), due to high accuracy, stability, and insensitivity to data shape and distribution.
412 This study utilizes area-weighted ordinary kriging algorithm to estimate the unknown values of AOD at
413 specific locations to generate gridded AOD. The longitude range is between -179.5° E and 180 °E, the
414 latitude range is between -60 °N and 85 °N, and the spatial resolution is 0.5 °*0.5 °.

415 **2.8 Evaluation metrics**

416 Evaluation metrics, including Root Mean Squared Error (RMSE), Mean Absolute Error (MAE) and

417 Pearson Correlation Coefficient (R), are used to measure the performance and accuracy of the model and
418 gridded results.

419 $$RMSE = \sqrt{\frac{1}{n}\sum_{i=1}^{n}(y_i - \hat{y}_i)^2} \quad \textbf{Eq. 11}$$

420 $$MAE = \frac{1}{n}\sum_{i=1}^{n}|y_i - \hat{y}_i| \quad \textbf{Eq. 12}$$

421 $$R = \frac{\sum_{i=1}^{n}(y_i - \bar{y})(\hat{y}_i - \bar{\hat{y}})}{sqrt(\sum_{i=1}^{n}(y_i - \bar{y})^2 \sum_{i=1}^{n}(\hat{y}_i - \bar{\hat{y}})^2)} \quad \textbf{Eq. 13}$$

422 where y_i and $\bar{y}$ are the predicted value and the average of the predicted values. $\hat{y}_i$ and $\bar{\hat{y}}$ are
423 the target and the average of the target. $i = 1,2,\ldots,n$. n is the length of sample.
424 The expected error (EE) is used to evaluate the AOD derived from visibility.
425 $$EE = \pm(0.05 + 0.15 * \tau_{target}) \quad \textbf{Eq. 14}$$
426 where τ_{target} is AERONET AOD or Terra MODIS AOD at 550nm.

427

428
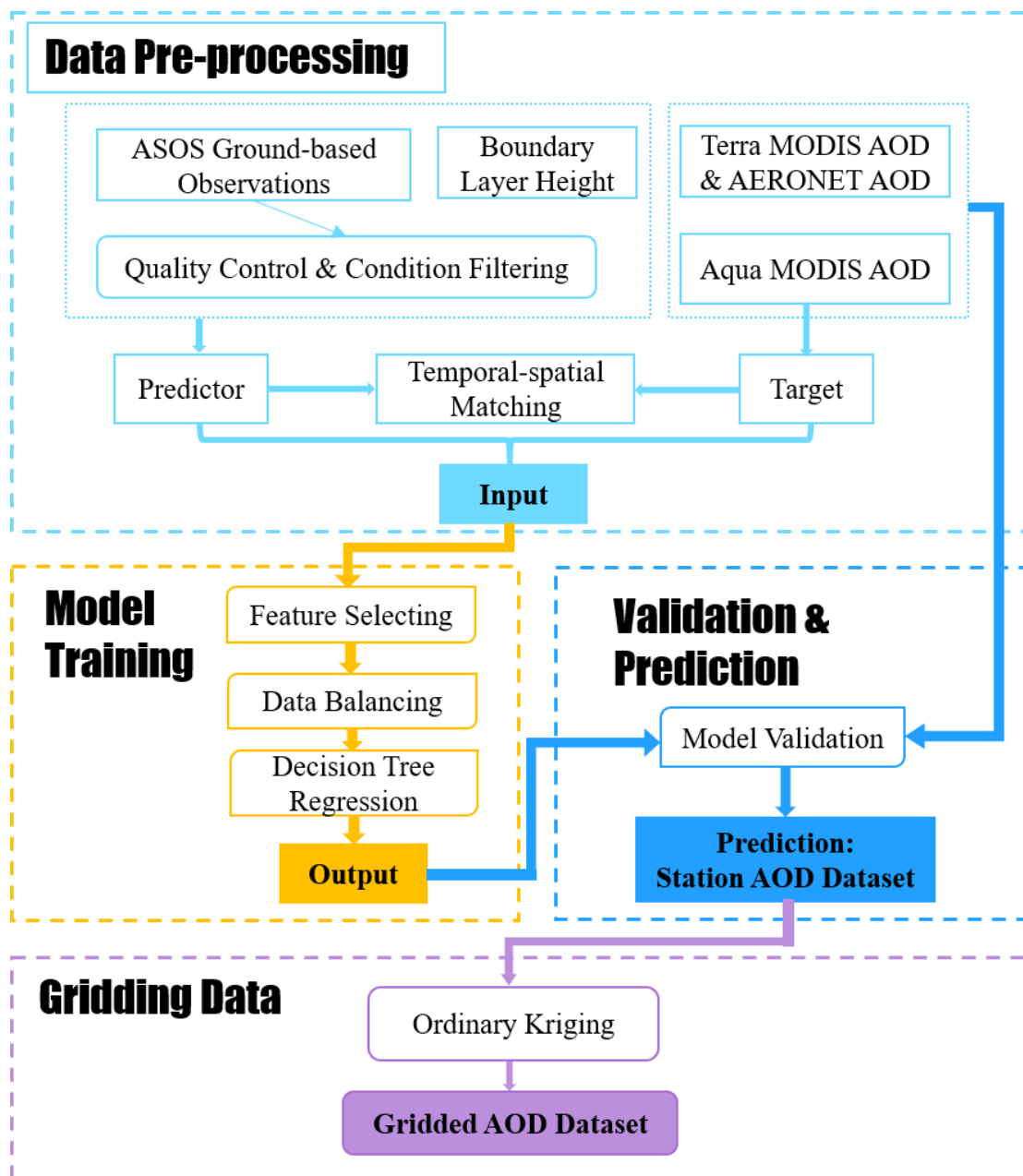
Figure 2 Flowchart for deriving aerosol optical depth (AOD).

2.9 Workflow

Figure 2 is the summarized flowchart and provides an overview of the structure of this study, which involves four main parts: (1) data preprocessing, (2) model training, (3) validation and prediction, and (4) data gridding.

3 Results and discussion

3.1 Dependence of model performance on training data length

436

437
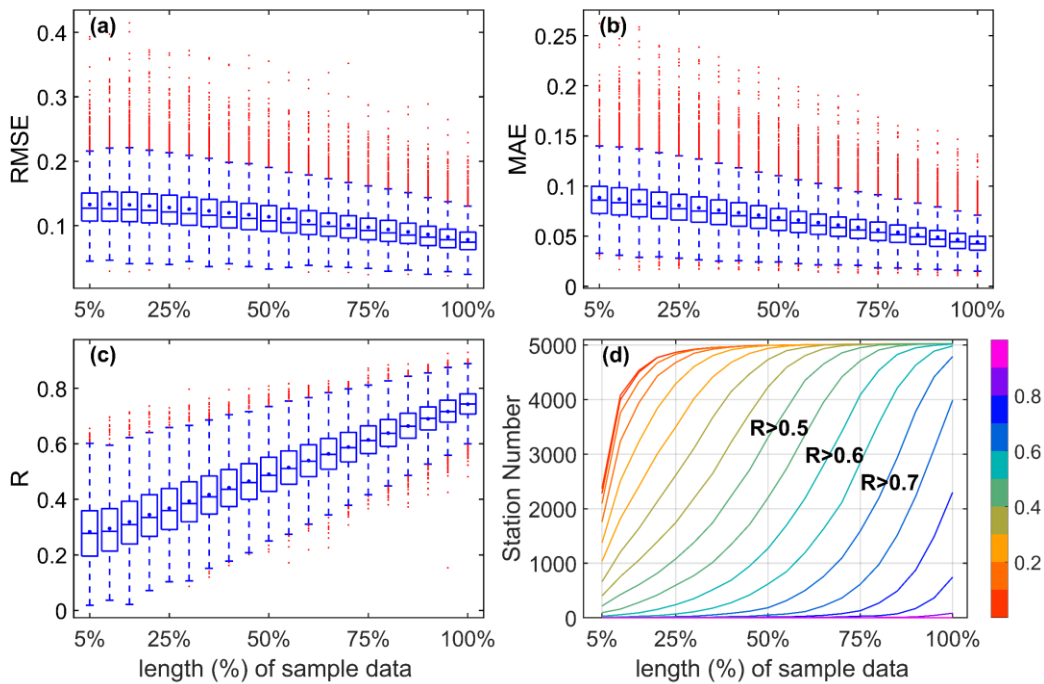
Figure 3 Boxplots of root mean squared error (RMSE) (a), mean absolute error (MAE) (b), and correlation coefficient (R) (c) between predicted values and target using different lengths of sample data (5% interval) as the training dataset, and the correlation coefficient curve (d) of the station number in the different lengths of sample data.

We build the models using different lengths of sample data (5% to 100%, with a 5% interval) by random allocation without overlap and evaluate the predictive performance of each model. Figure 3 depicts RMSE(a), MAE(b), and R (c) between the predicted values and target based on the training data of 5% to 100% sample data at a station. As the volume of the training data increases, the RMSE and MAE decrease, and the correlation coefficient increases. Compared to 5% of the sample data, the result of 100% sample data shows a decrease in RMSE by 41.1%, a decrease in MAE by 50.1%, and an increase in R by 162.3%. The relationship between the length of sample data and the model's performance is positive for each station. Figure 3 (d) shows that R of approximately 70% stations is greater than 0.5 at 50% of the sample data, while at 75%, the R of approximately 80% of stations is greater than 0.6. When 100% of the sample data is used as sample data, the R of approximately 80% of stations is greater than 0.75, and the R of about 97% is greater than 0.7. This finding indicates that the predictive capability and robustness of the model increase as the amount of training data increases. It may be attributed to the model's ability to capture more complex patterns and relationships among the input by multi-year data.

3.2 Evaluation of model training

Figure 4 shows the spatial distribution (a-c) and frequency and cumulative frequency (d-e) of RMSE, MAE, and R of all stations. The mean values of RMSE, MAE, and R are 0.078, 0.044, and 0.750, respectively. The RMSE of 93% stations is less than 0.11, the MAE of 91% is less than 0.06, and the R of 88% is greater than 0.7. The R values in Africa, Asia, Europe, North America, Oceania, and South America are 0.763, 0.758, 0.736, 0.750, 0.759, and 0.738, respectively. Although the RMSE and MAE of a few stations are high in America and Asia, the R is still high (>0.6). Therefore, the results of the

model's errors demonstrate that the model performs well on almost all stations.
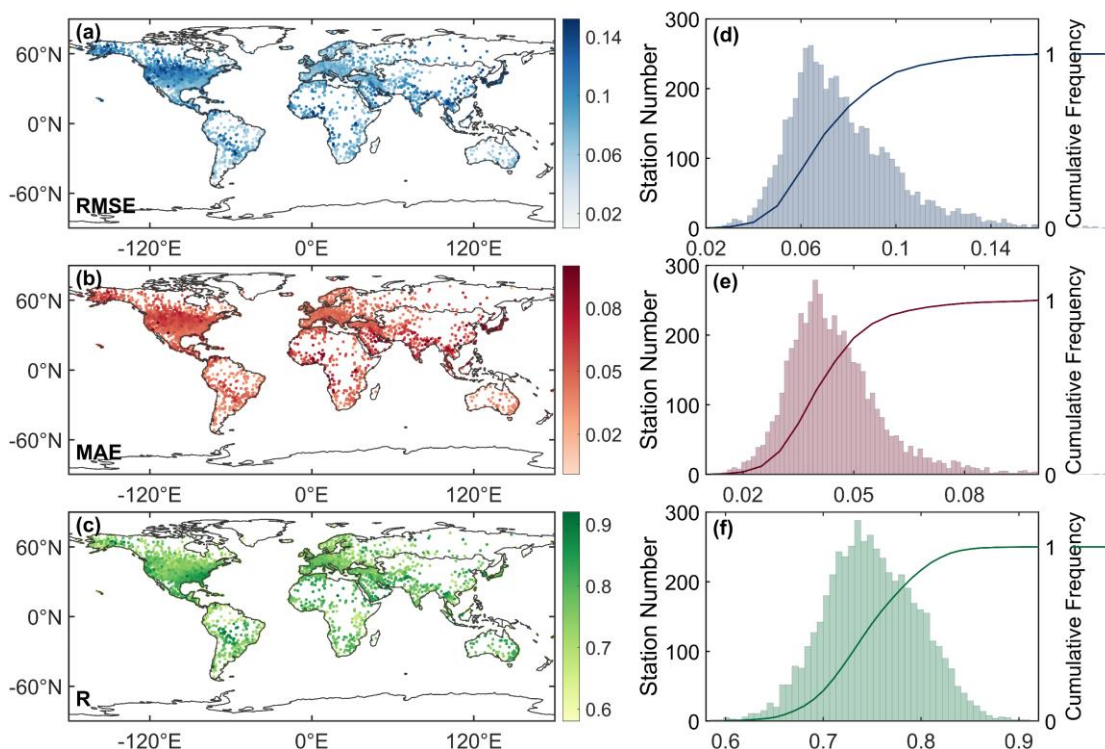
Figure 4 Spatial distribution (a-c) of root mean squared error (RMSE), mean absolute error (MAE), and correlation coefficient(R) between the model's result and target with 100% sample data. Station number (bar) and cumulative frequency (curve) (d-e) of RMSE, MAE, and R.

3.3 Validation and comparison with MODIS and AERONET AOD

3.3.1 Validation over global land

To validate the model's predictive ability, the visibility-derived AOD (for short, VIS_AOD) is compared with Aqua, Terra and AERONET AOD at 550nm for the global scale. Among them, Aqua AOD has been used as training data, which is not independent. Terra AOD and AERONET AOD have not been used as training data and can be regarded as independent data.

First, the relationship among daily MODIS and AERONET AOD is evaluated. Figure 5 shows the scatter density plots between AERONET AOD and Aqua AOD (a, d, g) and Terra AOD (b, e, h). The R values with Aqua AOD and Terra AOD are 0.643 and 0.637 on the daily scale, and 0.668 and 0.658 on the monthly scale, 0.658 and 0.665 on the yearly scale. The RMSE with Aqua AOD and Terra AOD are 0.158 and 0.163 on the daily scale, and 0.122 and 0.127 on the monthly scale, 0.101 and 0.103 on the yearly scale. The MAE values with Aqua AOD and Terra AOD are 0.084 and 0.088 on the daily scale, and 0.071 and 0.072 on the monthly scale, 0.061 and 0.062 on the yearly scale. The percentages of sample point falling within the EE envelopes are 64.66% and 62.54% on the daily scale, and 69.36% and 69.08% on the monthly scale, 74.80% and 75.89% on the yearly scale.
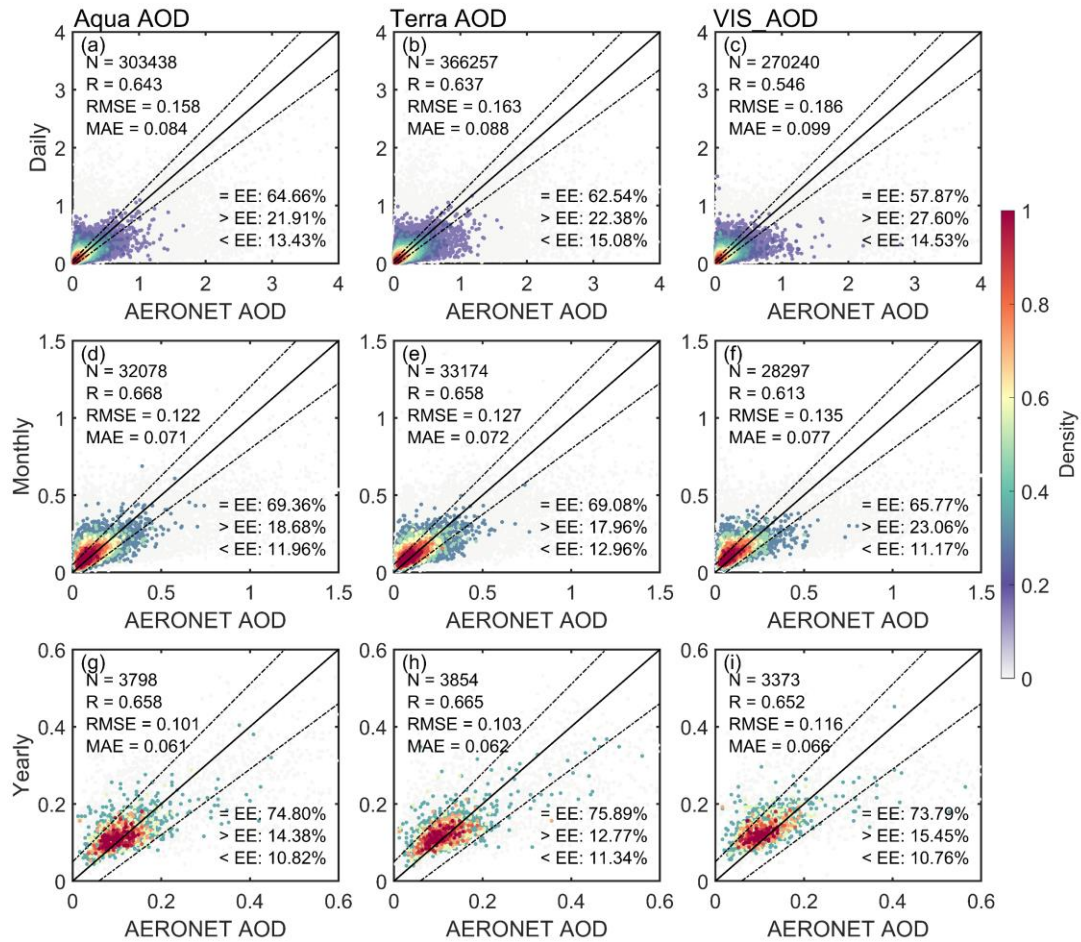
Figure 5 Scatter density plots between AERONET AOD (550nm) and Aqua MODIS AOD, Terra MODIS AOD and VIS_AOD at the daily (a-c), monthly (d-f) and yearly (g-i) scale. The solid black line represents the 1:1 line and the dashed lines represents expected error (EE) envelopes. The sample size (N), correlation coefficient (R), mean absolute error (MAE), and root mean square error (RMSE) are given. '=EE', '>EE', and '< EE' represent the percentages (%) of retrievals falling within, above, and below the EE, respectively. The matching time for Aqua AOD and VIS_AOD with AERONET AOD is 13.30 (± 30 minutes) at local time, and the matching time between Terra AOD and AERONET AOD is 10.30 (± 30 minutes) at local time.

Figure 6 shows the scatter density plots and the EEs between VIS_AOD and Aqua AOD, Terra AOD, and AERONET AOD. Aqua AOD is not an independent validation, and Terra and AERONET AOD are independent validation. For the daily scale, the R, RMSE and MAE of between VIS_AOD and Aqua AOD (15,962,757 pairs data) is 0.799, 0.079 and 0.044, respectively. The percentage of sample point falling within the EE envelopes is 84.12% on the global scale (Figure 6 a). The R between VIS_AOD and Terra AOD (17,145,578 pairs data) is 0.542, with a RMSE of 0.125 and MAE of 0.078. The percentage falling within the EE envelopes is 64.76% (Figure 6 b). The R between VIS_AOD and AERONET AOD (270,240 pairs data) at 397 sites is 0.546, with a RMSE of 0.186 and MAE of 0.099. The percentage falling within the EE envelopes is 57.87% (Figure 6 c).

For the monthly and annual scales, RMSE and MAE show a significant decrease between VIS_AOD and Aqua, Terra, and AERONET AOD, and R and percentages falling within EE show a significant increase

in Figure 6 (d-i). The monthly RMSEs are 0.029, 0.051, and 0.135, the monthly MAEs are 0.018, 0.031, and 0.077, and the R values are 0.936, 0.808, and 0.613, respectively. The percentages falling within the EE envelopes are 98.34%, 93.25%, and 65.77%. The RMSEs at the annual scale are 0.013, 0.024, and 0.116, the MAEs are 0.008, 0.015, and 0.066, and the R values are 0.976, 0.906, and 0.652, respectively. The percentages falling within the EE envelopes are 99.82%, 99.20%, and 73.79%. The percentage falling within the EE envelopes against AERONET is smaller than that against Terra, which may be related to the elevation of AERONET sites, the distance between AERONET and meteorological stations, and observed time. The results highlighted above demonstrate a clear improvement in performance on the monthly and annual scales compared to the daily scale (Schutgens et al., 2017), which provided a foundation for the gridded dataset.

On the daily, monthly, and annual scales, compared with AERONET AOD, the correlation coefficients, RMSE, MAE, and percentages falling within the expected error of VIS_AOD and MODIS AOD are very close. Since the time of AERONET AOD and VIS_AOD overlaps before 2000, it indicates that VIS_AOD also has the same accuracy.
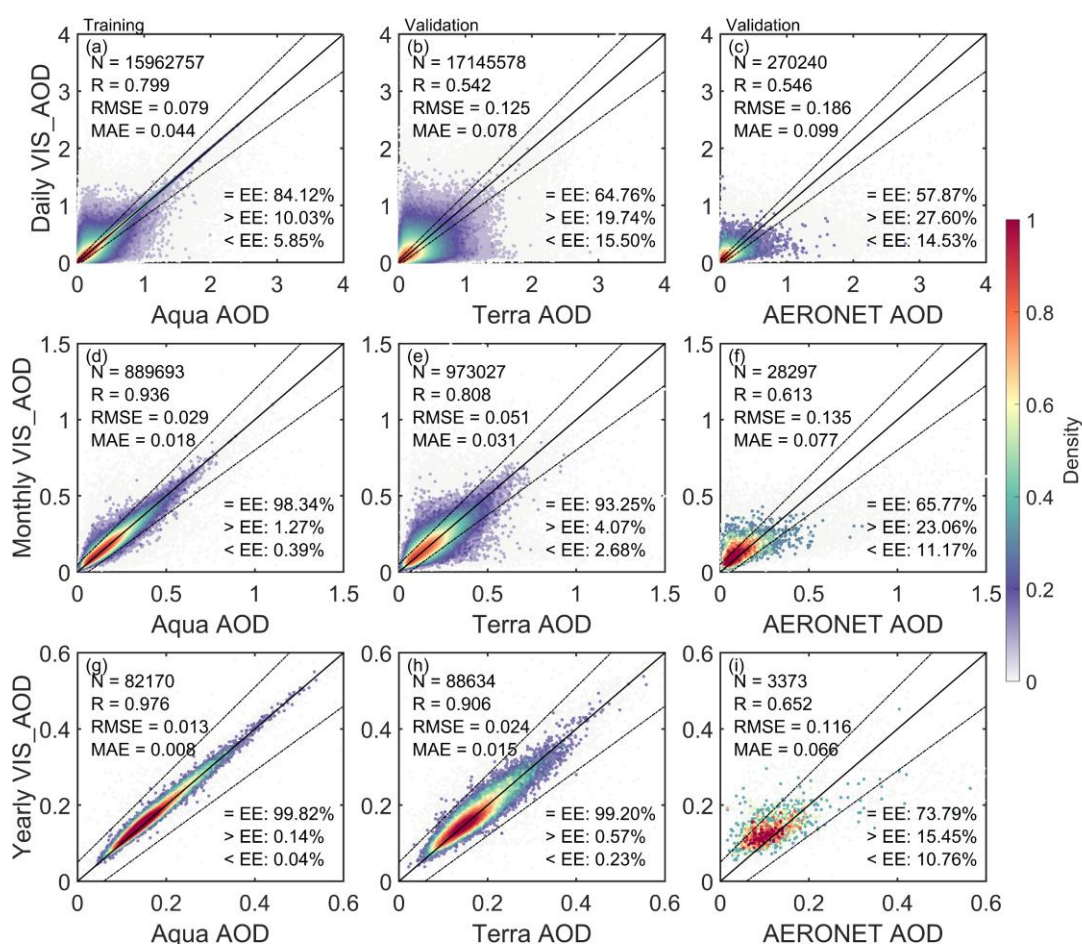
Figure 6 Scatter density plots between predicted AOD (VIS_AOD) and Aqua MODIS AOD, Terra MODIS AOD and AERONET AOD at the daily (a-c), monthly (d-f) and yearly (g-i) scale. The solid black line represents the 1:1 line and the dashed lines represents expected error (EE) envelopes. The sample size (N), correlation coefficient (R), mean absolute error (MAE), and root mean square error (RMSE) are given. '=EE', '>EE', and '< EE' represent the percentages (%) of retrievals falling within, above, and below the EE, respectively. Note Aqua AOD is not an independent validation for predicted

524   results, while Terra and AERONET are independent validation.

525   **3.3.2 Validation over regions**

526   Aerosol loading exhibits spatial variability. Evaluation metrics for the relationships between
527   visibility-derived AOD and AERONET AOD and Terra AOD for each region are listed in Table 1.
528   Over Europe and North America, the results are similar to those of Terra and AERONET, with a
529   large number of data pairs, greater than 10^5 (AERONET) and greater than 10^7 except for Eastern
530   Europe (Terra) on the daily scale. Approximately 63% -70% fall within the EE envelopes. The
531   RMSE is approximately 0.1100, except for western North America, the MAE is approximately
532   0.0700, with a correlation coefficient between 0.44 and 0.54.
533   Over Central South America, South Africa, and Australia, data pairs are about $10^{3\text{-}4}$ (AERONET)
534   and 10^6 (Terra) on the daily scale. 52-60% fall within the EE envelopes compared to AERONET,
535   and 58-67% compared to Terra. The RMSE is 0.03-0.05 compared to Terra, and 0.11-0.17 compared
536   to AERONET. The correlation coefficient ranges from 0.4 to 0.74, with the highest correlation
537   coefficient in South America at 0.740.
538   In Asia, India, and West Africa, the data pairs are only approximately 10^4 (AERONET). 32% to 50%
539   fall within the EE envelopes compared to AERONET, the RMSE ranges from 0.2 to 0.5, and the
540   MAE ranges from 0.11 to 0.36. 51 to 58%, compared to Terra, fall within the EE envelopes, the
541   RMSE is around 0.16, and the MAE is around 0.11. Compared to AERONET, in these high aerosol
542   loading regions, RMSE and MAE increase, and the percentages falling within the EE envelopes
543   decrease, but the correlation coefficients do not significantly decrease.
544   Compared to Terra AOD, 55% -67% of data falls within the EE envelopes on the daily scale, 87% -
545   96% on the monthly scale, and over 97% on the yearly scale. Compared to AERONET AOD, 32-
546   68% of data falls within the EE envelopes, 24% -84% on the monthly scale, and 15% -97% on the
547   yearly scale. On both monthly and yearly scales, all metrics have shown a significant increase in
548   performance when compared to Terra. However, compared to AERONET, not all metrics increase
549   in some regions due to limited data pairs, such as West Africa, Northeast Asia, and India, which may
550   be due to the spatial differences between AERONET sites and meteorological stations.
551   Overall, the AOD from visibility is more effective in regions such as Europe and North America,
552   which may also be related to the better performance of the MODIS DT algorithm in vegetation-
553   covered regions. In high aerosol load areas affected by deserts, such as Africa and Asia, the AOD of
554   visibility inversion needs to be improved.

555   **3.3.3 Validation at a site scale**

556   Sites, especially AERONET, are not completely uniform across the word or in any region, and
557   different stations have different sample sizes, which may lead to a certain uncertainty. Therefore,
558   further analysis was conducted on the spatial distribution of different evaluation metrics. Figure 7
559   shows the validation and comparison of daily VIS_AOD against Terra and AERONET AOD at a
560   site scale.
561   Compared to Terra daily AOD, the R of 67% stations is greater than 0.4, the mean bias of 83% is

562 **Table 1** Evaluation metrics for the relationships between visibility-derived AOD and AERONET AOD and Terra AOD for each region.

Region		N			R			RMSE			MAE			Within EE (%)		
		daily	monthly	yearly	daily	monthly	yearly	daily	monthly	yearly	daily	monthly	yearly	daily	monthly	yearly
Eastern Europe	AERONET	21724	2317	271	0.463	0.493	0.653	0.1069	0.0647	0.0326	0.0714	0.0442	0.0263	65.69	83.77	97.42
	TERRA	661630	36435	3278	0.464	0.665	0.790	0.1095	0.0471	0.0214	0.0726	0.0286	0.0122	66.07	94.71	99.18
Western Europe	AERONET	53043	6033	697	0.445	0.487	0.344	0.1089	0.0716	0.0513	0.0711	0.0474	0.0347	64.40	79.21	89.10
	TERRA	1778013	104620	9166	0.467	0.763	0.811	0.1096	0.0391	0.0210	0.0712	0.0268	0.0124	66.99	95.42	99.40
Western North America	AERONET	33859	2948	334	0.503	0.484	0.509	0.1465	0.0949	0.0566	0.0747	0.0597	0.0419	63.58	67.37	81.14
	TERRA	1725226	82734	7201	0.542	0.765	0.906	0.1144	0.0465	0.0180	0.0671	0.0267	0.0125	69.48	94.42	99.61
Eastern North America	AERONET	47407	5359	608	0.527	0.526	0.559	0.1135	0.0824	0.0436	0.0657	0.0472	0.0331	67.52	77.78	87.50
	TERRA	6280277	359520	31343	0.515	0.799	0.847	0.1159	0.0435	0.0165	0.0726	0.0275	0.0111	66.70	94.94	99.80
Central South America	AERONET	10911	1176	149	0.740	0.811	0.866	0.1735	0.1272	0.1060	0.1021	0.0904	0.0688	52.40	47.96	67.79
	TERRA	444780	26362	2410	0.545	0.820	0.776	0.1447	0.0591	0.0369	0.0909	0.0396	0.0219	58.48	89.29	97.39
Southern Africa	AERONET	4255	309	38	0.423	0.480	0.630	0.1553	0.1128	0.0705	0.1033	0.0805	0.0525	52.08	59.55	78.95
	TERRA	216239	11304	1118	0.518	0.821	0.870	0.1258	0.0511	0.0296	0.0836	0.0340	0.0191	60.64	91.70	98.21
Australia	AERONET	6426	516	63	0.488	0.654	0.363	0.1094	0.0827	0.0725	0.0711	0.0620	0.0563	59.96	59.88	71.43
	TERRA	284693	14588	1286	0.398	0.784	0.831	0.1091	0.0363	0.0188	0.0666	0.0261	0.0143	67.01	94.65	99.38
Western Africa	AERONET	2205	205	34	0.553	0.594	0.762	0.3180	0.2873	0.3357	0.2082	0.2029	0.2587	37.96	40.00	23.53
	TERRA	156392	10468	1028	0.501	0.769	0.849	0.1769	0.0706	0.0412	0.1198	0.0482	0.0242	51.83	88.01	97.57
Southeast Asia	AERONET	4134	504	74	0.405	0.542	0.488	0.2037	0.1447	0.1198	0.1274	0.0988	0.0821	50.17	56.15	60.81
	TERRA	402465	27058	2500	0.470	0.753	0.872	0.1730	0.0729	0.0342	0.109	0.0455	0.0198	57.25	87.01	97.96
Eastern China	AERONET	7396	927	118	0.513	0.551	0.356	0.3571	0.2355	0.1933	0.2038	0.1392	0.1382	40.10	49.84	50.00
	TERRA	241185	17324	1518	0.523	0.811	0.895	0.1646	0.0638	0.0302	0.1073	0.0435	0.0225	55.77	88.07	98.88
Northeast Asia	AERONET	9979	1178	142	0.569	0.593	0.367	0.4941	0.3249	0.2604	0.2924	0.2425	0.2202	35.17	29.54	21.13
	TERRA	78823	5485	467	0.553	0.872	0.965	0.1973	0.0636	0.0263	0.1201	0.0440	0.0198	56.48	87.77	98.29

| India | AERONET | 2208 | 203 | 32 | 0.521 | 0.462 | 0.534 | 0.2957 | 0.3015 | 0.3588 | 0.2049 | 0.2283 | 0.2862 | 32.11 | 24.63 | 15.63 |
| | TERRA | 179928 | 9564 | 862 | 0.526 | 0.815 | 0.915 | 0.1564 | 0.0599 | 0.0352 | 0.1089 | 0.042 | 0.0238 | 55.16 | 90.43 | 98.14 |

563

less than 0.01, the RMSE of 85% is less than 0.15, and the percentage falling within the EE of 67% is greater than 60%. More than 85% of stations fall within the EE is greater than 60% in Europe, North America, and Oceania, while 40-60% in South America, Africa, and Asia. The percentage of expected error is low in South and East Asia, and Central Africa, with some underestimation. Above 60% in Africa, Asia, North America, and Europe have a correlation coefficient greater than 0.4. The regions with lower correlation are the coastal regions of South America, eastern Africa, western Australia, northeastern North America, and northern Europe. Above 90% of the RMSE in Europe, North America, and Oceania have a correlation coefficient smaller than 0.15. High RMSE regions are in western North America, Asia, central South America, and central Africa.

Compared to AERONT daily AOD, the R of 74% stations is greater than 0.4, and the spatial distribution is similar to Terra's. The mean bias of 44% is less than 0.01, the RMSE of 68% is less than 0.15, and the percentage falling within the EE of 53% is greater than 60%. More than 70% of sites have a correlation coefficient greater than 0.4 in Africa, Asia, Europe, and North America. More than 57% of sites have an expected error percentage of over 60% in Europe, North America, and Oceania. Except for Asia. Over 72% of sites have a RMSE less than 0.15. Except for Oceania and South America, over 71% of sites in other regions have MAE less than 0.01. Almost all sites in Asia show a negative bias, significantly underestimating. However, there is a significant overestimation in western North America and western Australia. Most sites in Asia falling within the expected error are less than 50%. High RMSE region are in Asia, India, and central Africa.

The validation and comparison on the site scale show a limitation similar to the MODIS DT algorithm. In areas with high vegetation coverage, the AOD from visibility are better than those in bright areas such as deserts.
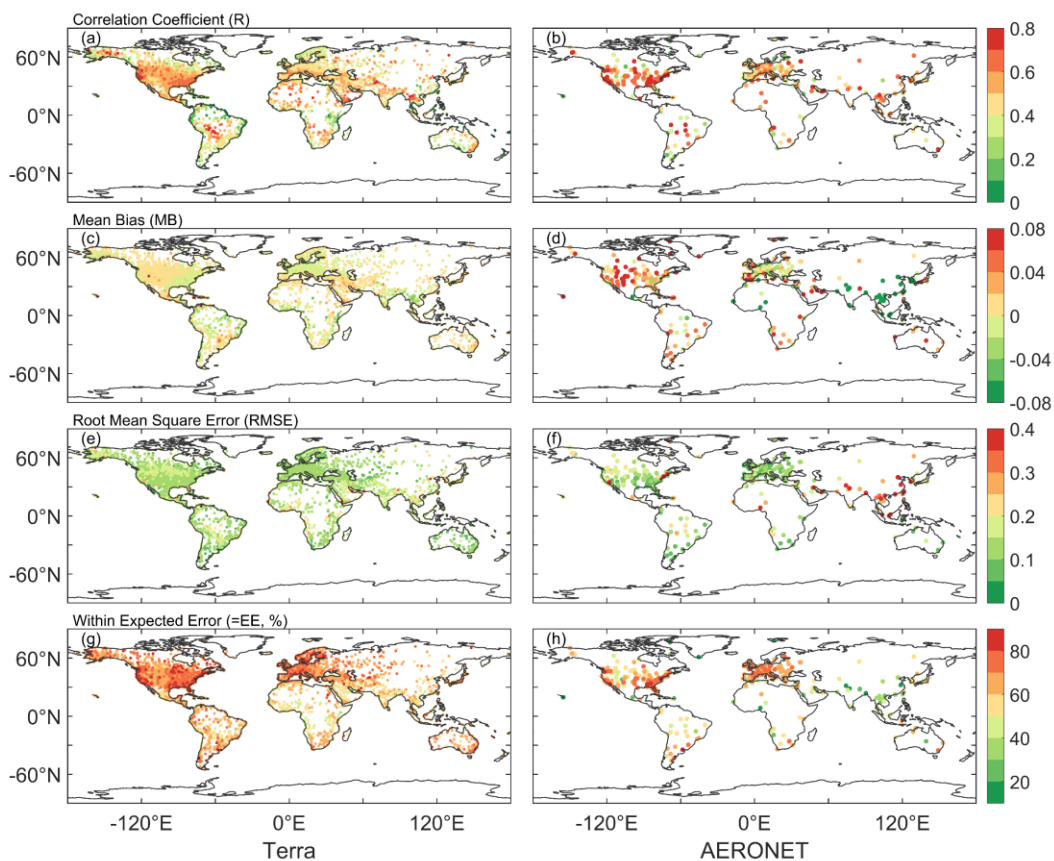
Figure 7 Validation of VIS_AOD against Terra and AERONET AODs at each site: (a–b) correlation (R), (c-d) mean bias (MB), (e-f) root mean square error (RMSE), (g-h) percentage (%) of VIS_AOD within the expected error envelopes.

3.3.4 Discussion and uncertainty analysis

The atmospheric visibility is a horizontal physical quantity, while AOD is a column-integrated physical quantity. We have linked the two variables together using machine learning methods, which partially compensates for the scarcity of AOD data. However, we have to face some limitations. Although the boundary layer height is considered, it is not sufficient. Pollutants such as smoke from biomass burning, dust, volcanic ash, and gas-aerosol conversion of sulfur dioxide to sulfate aerosols in the upper and lower troposphere can undergo long-range aerosol transport under the influence of circulation. The pollution transport and aerosol conversion processes above the boundary layer are still significant and cannot be ignored (Eck et al., 2023). Compared to surface visibility, bias occurs when the aerosol layer rises and affects AERONET measurements and MODIS retrievals. Therefore, it should be considered when using this data. If there were sufficient historical vertical aerosol measurements with high temporal and spatial resolution, the results of this data would be greatly improved. Although some studies use aerosol profiles from pollution transport models or assumed profiles as substitutes for observed profiles (Li et al., 2020; Zhang et al., 2020), the biases introduced by these non-observed profiles are still significant.

In machine learning, we used MODIS Aqua AOD as the target value for the model because the validation results for MODIS C6.1 products have a correlation coefficient of 0.9 or higher with AERONET AOD at the daily scale (Wei et al., 2019; Wei et al., 2020). Compared to AERONET, MODIS AOD provides more sample data with a high global coverage. However, apart from modeling errors, the systematic biases and uncertainties of MODIS Aqua AOD cannot be ignored (Levy et al., 2013; Levy et al., 2018; Wei et al., 2019). Averaging over time scale significantly reduces systematic errors but cannot diminish errors caused by emission sources and terrain. Therefore, the strong correlation at monthly and annual scales indicates a substantial reduction in errors (Schutgens et al., 2017). This is also one of the reasons why this dataset shows stronger correlation with Terra AOD and weaker correlation with AERONET in validation.

The spatial matching between meteorological stations and AERONET sites may cause some biases. AERONET sites are usually not co-located with meteorological stations in terms of elevation and horizontal distance, this is another reason for the weak correlation between VIS_AOD and AERONET AOD. The meteorological stations are located at the airport. Different horizontal distances may result in meteorological stations and AERONET sites being located on different surfaces (such as urban, forest, mountainous). Differences in site elevation significantly impact the relationship between AOD and measured visibility. When the AERONET site is at a higher elevation than the meteorological station, there may be fewer measurements of aerosols over the sea at the AERONET site.

Different pollution levels and station elevation affect the AOD derived from visibility. The elevation difference and distance between meteorological stations and AERONET sites also have an impact on the validation results. Therefore, the error and performance of different AERONET AOD values, station elevation, and distance were analyzed.

3.3.4.1 Uncertainty with pollution level

As the AOD increases, the variability of bias also increases in Figure 8 (a). Almost all mean bias values are within the envelope of EE, except for 1.1-1.2 and 1.5-1.6. The average bias is 0.015 (AOD <0.1), with 83% of data within the EE envelopes. The mean bias is -0.0011 (AOD,0.1-0.2), with 54% within the EE envelopes. The mean bias is negative (AOD, 0.3-1.0), with 20%-40% falling within the EE envelopes. There is a positive bias (AOD, 1.1, 1.4 and >1.6), and there is a negative bias at 1.2-1.3 and 1.5-1.6. The results indicate that as pollution level increases, the negative mean bias becomes significant and the underestimation increases.

3.3.4.2 Uncertainty with elevation of AERONET site

The contribution of particulate matter near the ground to the column aerosol loading is significant. The elevation of the site affects the measurement of column aerosol loading in Figure 8 (b). There is a negative bias in the low elevation (<=0.5km) with a percentage of 60%-64% falling within the EE envelopes and a positive bias in high elevation (0.5-1.2km) with a percentage of 50%-65% falling within the EE envelopes. The percentage significantly decreases (>1.2km), and the average bias increases. Therefore, the elevation of AERONET's site will cause bias in validation, and. the uncertainty greatly increases in high elevation.

3.3.4.3 Uncertainty with elevation of meteorological station

Due to the elevation difference between the meteorological station and AERONET site in the vertical direction, the uncertainty caused by elevation differences of site was analyzed in Figure 8 (c). When the elevation difference is negative (the elevation of the meteorological station is lower than that of the AERONET station), there is a significant positive bias. When the difference is positive, the mean bias approaches 0 or is positive. The percentage is greater than 60% (-0.5 km-0.5km). The positive mean bias is greater than the negative mean bias, and the uncertainty greatly increases when the elevation of meteorological stations is lower than that of AERONET sites. It indicates that the contribution of the near surface aerosol to the column aerosol loading is significant and cannot be ignored.

3.3.4.4 Uncertainty with distance between meteorological station and AERONET site

The spatial variability of aerosols is significant. Meteorological stations and AERONET sites are not collocated, resulting in a certain distance in spatial matching. In this study, the upper limit of distance is 0.5 degree. Figure 8 (d) shows the error of the distance between stations, where the degree is converted to the distance at WGS84 coordinates. The bias does not change significantly with increasing distance. The average bias is around 0, with the maximum positive mean bias (0.0322) at a distance of 2km and the maximum negative mean deviation (-0.0323) at 6km. The median is almost positive, except at 5km and 6km. The percentage falling within the EE envelopes is over 50%, with the maximum percentage (66%) at 3km and the minimum (62%) at 2km.

663
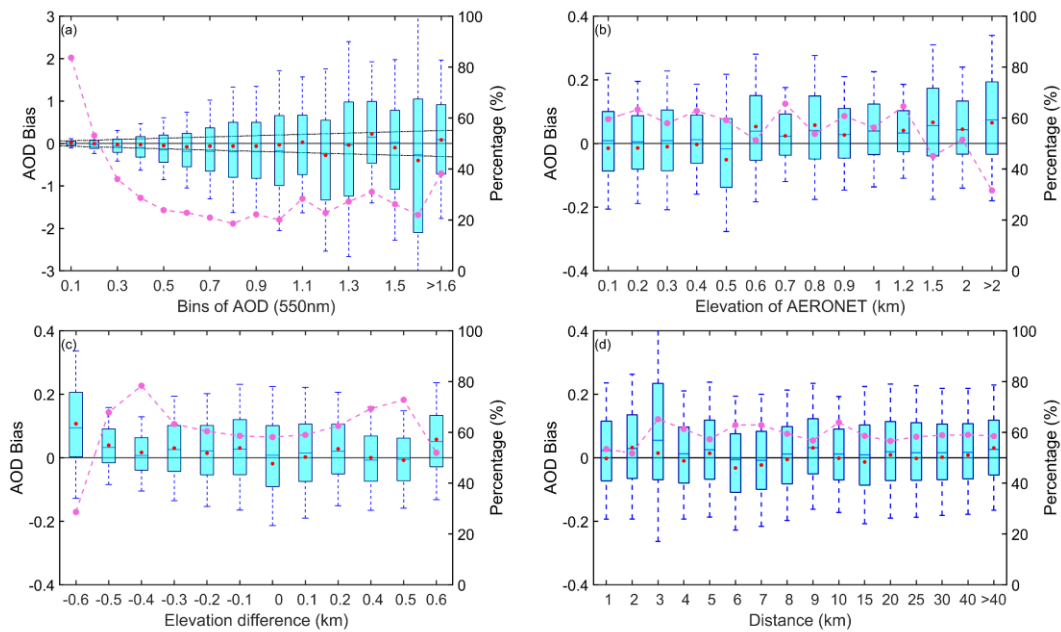
Figure 8 Box plots of AOD bias and the percentage falling within the EE envelopes (curves): (a) AERONET AOD levels, (b) elevation of AERONET sites, (c) elevation difference between meteorological stations and AERONET sites, (d) distance (km) between meteorological stations and AERONET sites. The black horizontal line represents the zero bias. For each box, the upper, lower, and middle horizontal lines, and whiskers represent the AOD bias 75th and 25th percentiles, median, and 1.5 times the interquartile difference, respectively. The black solid lines represent the EE envelopes ($\pm(0.05+0.15*AOD_{AERONET})$). No site with a difference of +0.3km (x-axis label without 0.3) in (c).

3.4 Gridded visibility-derived AOD

Figure 9 shows the gridded AOD based on ordinary kriging interpolation with the area-weighted method and compares the multi-year spatial, zonal, and meridional distributions of AOD with Aqua and Terra AOD over land from 2003 to 2021. The VIS_AOD is 0.157±0.073 over land, which is almost equal to the Aqua (0.152±0.084) and Terra (0.154±0.088) AOD values with relative biases of 3.3%, and 1.9%, respectively. In order to compare the spatial correlation, Aqua and Terra MODIS AOD are averaged to the 0.5-degree resolution. In the heatmap (Figure 10), the R of VIS_AOD and Aqua AOD is 0.798, the RMSE is 0.049 with a bias of 32% compared to the mean, and the MAE is 0.008, with a bias of 5% compared to the mean. Compared to Terra AOD, the R is 0.787, and the RMSE is 0.051, with a bias of 33% compared to the mean, and the MAE is 0.005, with a bias of 3% compared to the mean. The R between Aqua and Terra AOD is 0.980. The R values between VIS_AOD and Aqua and Terra AOD are 0.995 and 0.990 for the zonal distribution and 0.986 and 0.897 for the meridional distribution, respectively. In the low aerosol loading region, VIS_AOD exhibits a little overestimation. Whether in meridional or zonal distribution, the peak and valley regions are basically consistent (Tian et al., 2023). Due to the limitations of satellite inversion algorithms, a bias appears on the bright surface, especially in northern North America with extensive snow cover (Levy et al., 2013). All above results suggest that the gridded AOD is consistent with satellite observations in spatial distribution.

690

691
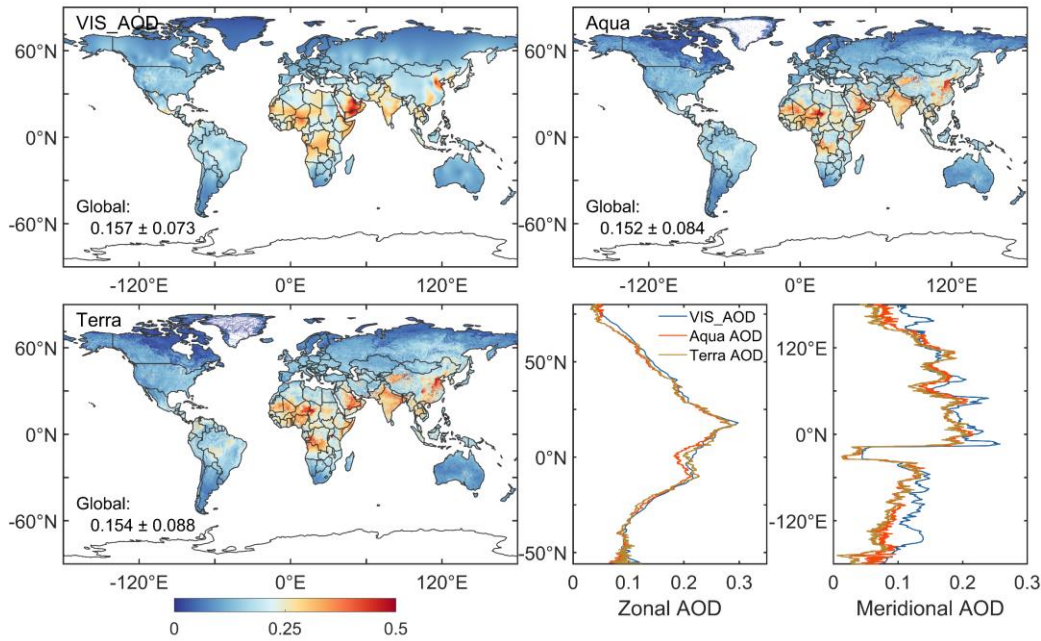
Figure 9 The spatial, zonal and meridional distributions of the multi-year mean VIS_AOD, Aqua
AOD, and Terra AOD over land from 2003 to 2021.

694

695
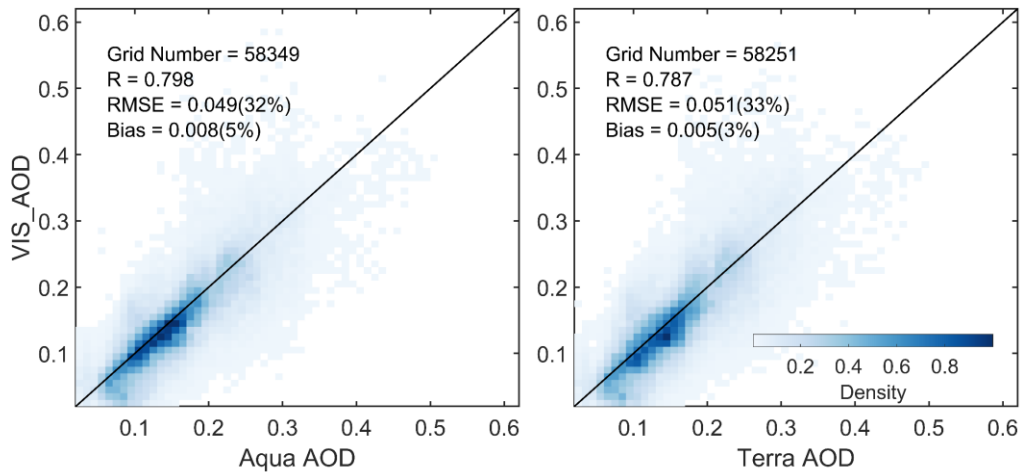
Figure 10 Heatmap of multi-year mean gridded VIS_AOD and Aqua AOD and Terra AOD during
2003-2021. Terra and Aqua AOD are averaged onto a grid of 0. 5°.

3.5 Interannual variability and trend of visibility-derived AOD over global land

The spatial distribution of multi-year average AOD from 1980 to 2021 over land is shown in Figure
11 (a). The mean AOD of land (-60-85°N), Northern Hemisphere (NH, 0-85°N), and the Southern
Hemispheres (SH, -60-0°N) is 0.161 ± 0.074, 0.158 ± 0.076, and 0.173 ± 0.059, respectively. The
AOD values of Africa, Asia, Europe, North America, Oceania, and South America are 0.241, 0.222,
0.110, 0.111, 0.129 and 0.117, respectively.

704   Due to the influence of geography, atmospheric circulation, population, and emissions, the AOD
705   varies in different latitudes. Figure 12 illustrates the multi-year average AOD in different latitude
706   ranges for land, the NH, and the SH from 1980 to 2021. Within [-20, 20°N], the global average AOD
707   reaches its maximum (0.234), and the maximum AOD NH is 0.256 in [0, 20°N]. The highest AOD
708   in SH is 0.217 in in [-15, 0°N]. The average AOD in SH rapidly decreases from -15°N to -35°N. In
709   NH, AOD is generally greater than in SH from 5°N to 65°N. When, the latitude is greater than 70°N,
710   the NH's AOD is smaller than the SH's.

711   There are many regions of high AOD values occur in NH, with the distribution of population density.
712   Approximately 7/8 of the global population resides in the NH, with 50% concentrated at 20°N-40°N
713   (Kummu et al., 2016), indicating a significant impact of human activities on aerosols. The highest
714   AOD values are observed near 17°N, including the Sahara Desert, Arabian Peninsula, and
715   southeastern India, suggesting that in addition to anthropogenic sources, deserts also play a crucial
716   role in aerosol emissions. Lower AOD regions of the SH are from 25°S to 60°S, encompassing
717   Australia, southern Africa, and southern South America, indicating lower aerosol burdens in these
718   areas. Additionally, North America also exhibits low aerosol loading. Chin et al. (2014) analyzed
719   the AOD over land from 1980 to 2009 with the Goddard Chemistry Aerosol Radiation and Transport
720   model, which is similar to the visibility-derived AOD. The spatial distribution is consistent with the
721   satellite results (Remer et al., 2008; Hsu et al., 2012; Hsu et al., 2017; Tian et al., 2023). The AOD
722   and extinction coefficient retrieved from visibility show a similar distribution at global scale, with
723   a correlation coefficient of nearly 0.6 (Mahowald et al., 2007). Similar global (Husar et al., 2000;
724   Wang et al., 2009) and regional (Koelemeijer et al., 2006; Wu et al., 2014; Boers et al., 2015; Zhang
725   et al., 2017; Zhang et al., 2020) spatial distributions have been reported.

726   AOD loadings exhibit significant seasonal variations worldwide, particularly over land. In this study,
727   a year is divided into four parts: December-January-February (DJF), March-April-May (MAM),
728   June-July-August (JJA), and September-October-November (SON), corresponding to winter
729   (summer), spring (autumn), summer (winter), and autumn (spring) in NH (SH), respectively. Figure
730   11 (b-e) also depicts the spatial distribution of seasonal average AOD over land from 1980 to 2021.
731   The global AOD in DJF, MAM, JJA, and SON is 0.158±0.062, 0.162±0.081, 0.175±0.093, and
732   0.153± 0.070, respectively. The standard bias of AOD in JJA and MAM are greater than those in
733   DJF and SON. AOD exhibits seasonal changes, with the highest in JJA, followed by MAM, DJF,
734   and SON. From 1980 to 2021, the seasonal AOD in NH is 0.152±0.064 (DJF), 0.161±0.088 (MAM),
735   0.176±0.090 (JJA), and 0.144±0.060 (SON), and in SH is 0.184±0.041 (DJF), 0.166±0.044 (MAM),
736   0.169±0.072 (JJA), and 0.19±0.060 (SON).

737   In NH, the AOD ranking from high to low in season is summer > spring > winter > autumn. In SH,
738   the AOD ranking from high to low in season is spring > summer > winter > autumn. The highest
739   AOD is observed during JJA in NH, while in SH, the peak occurs during SON. The occurrence of
740   high AOD values is highly associated with the growth of hygroscopic particle and the photochemical
741   reaction of aerosol precursors under higher relative humidity in Asia (JJA) (Remer et al., 2008) and
742   Europe such as Russia (JJA), and biomass burning in South America (SON), Southern Africa (SON),
743   and Indonesia (SON) (Ivanova et al., 2010; Krylov et al., 2014). On the other hand, the lowest global
744   AOD values are observed during autumn, which may be attributed to the weakening of monsoon
745   systems (Li et al., 2016; Zhao et al., 2019).

In addition to the spatial characteristics of AOD, the temporal variations in AOD have also been of great interest due to the significant relationship between aerosols and climate change. Figure 11 (f) shows the temporal trends of annual average AOD (** represents passing the significance test, $p<0.01$) over the global land, the SH and the NH during 1980-2021. The global land, NH, and SH trends demonstrate decreasing trends of AOD with values of -0.0026/10a, -0.0018/10a, and -0.0059/10a, respectively, with all passing the significance test with a confidence level of 95%. Notably, the declining trend is much greater in the SH than in the NH. It may be related to the decrease in the frequency of sandstorms and wildfires and the increase in precipitation, such as in Australia. Two AOD peaks in 1983 and 1994 and two AOD valleys in 1980 and 1990 are observed before 2000. The two AOD peaks may be attributed to large volcanic eruptions, which has been confirmed by previous studies. The volcanic eruptions and their associated fires of the El Chichón volcano in Mexico in 1982 (Hirono and Shibata, 1983) and Mount Pinatubo in the Philippines in 1991(Tupper et al., 2005) resulted in elevating global AOD levels in the following years. The AOD recovery to the previous low levels after volcanic eruptions takes approximately 10 years (Chazette et al., 1995; Sun et al., 2019). This further indicates the efficiency of our data capturing the volcanic eruption emission features.

Due to the influence of geography, atmospheric circulation, population, and emissions, the trend of global aerosols varies in different latitude Figure 12 illustrates the multi-year average AOD in different latitude ranges for land, the NH, and the SH from 1980 to 2021. Within [-20, 20°N], the global average AOD reaches its maximum (0.234), and the maximum AOD NH is 0.256 in [0, 20°N]. The highest AOD in SH is 0.217 in in [-15, 0°N]. The average AOD in SH rapidly decreases from -15°N to -35°N. In NH, AOD is generally greater than in SH from 5°N to 65°N. When, the latitude is greater than 70°N, the NH's AOD is smaller than the SH's, which may be related to low emission intensity and low population density in high latitude areas.

The seasonal trends of AOD during 1980-2021 at the global and hemispheric scales are shown in Figure 11 (g-j). The global AOD shows a decreasing trend in all seasons (-0.002~-0.003/10a). The large declining trends are observed in JJA and SON, with decreasing trend values of -0.003/10a and -0.0029/10a, respectively. DJF and MAM follow with decreasing trend values of -0.0026/10a and -0.0022/10a, respectively, all passing the significance test ($p<0.01$). For the NH, the AOD trends in different seasons are -0.0030/10a (DJF), -0.0006/10a (MAM), -0.0005/10a (JJA), and -0.0034/10a (SON). DJF and SON pass the significance test ($p<0.01$), while MAM and JJA do not. In the SH, the trends are as follows: -0.0011/10a (DJF), -0.0085/10a (MAM), -0.0131/10a (JJA), and -0.0009/10a (SON). Interestingly, in contrast to the NH, MAM and JJA pass the significance test, while DJF and SON do not. The largest declining season in the NH is winter, while in the SH, it is summer. The decreasing trend in the SH is more than four times greater than that in the NH, particularly before the year 2000. While both the global and SH AOD exhibit a decreasing trend since 2005, the NH has shown a significant increase in winter AOD, leading to an overall increasing trend. Moreover, the NH shows an increasing trend of 0.004/10a from 2005 to 2021.

Annual SO_2 emissions increased from 9.4 to 15.3 TgS from 2000 to 2005, which ultimately ended up as sulfate aerosols, leading to a significant increase in sulfate aerosols (Hofmann et al., 2009). More relevantly, the frequent volcanic eruptions in tropical regions from 2002 to 2006, combined with seasonal circulation patterns during winter, led to the transport of aerosol particles to higher latitudes (Hofmann et al., 2009; Vernier et al., 2011; Sawamura et al., 2012; Andersson et al., 2015).

789

790
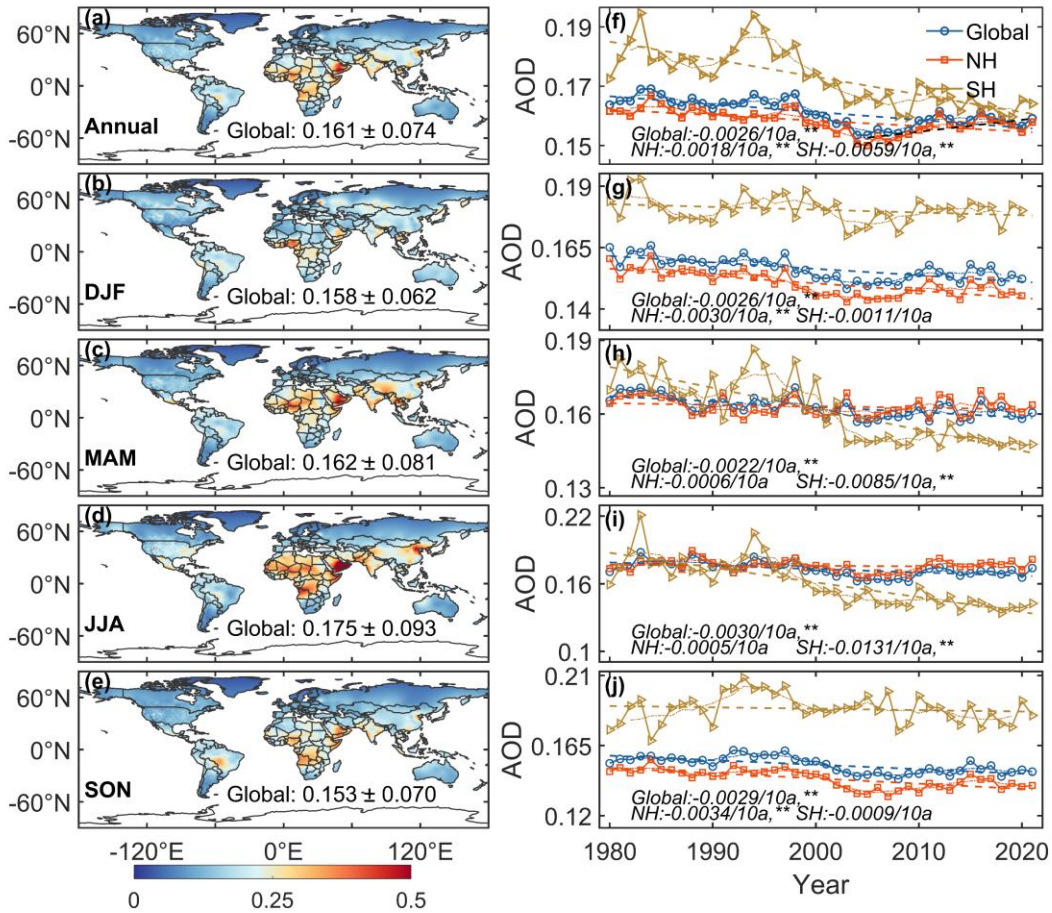
Figure 11 The multi-year averages of VIS_AOD from 1980 to 2021. Global land (circle), northern hemisphere (NH,0-85°N) (triangle) and southern hemisphere (SH,0-60°S) (square) annual and seasonal AOD. The symbol, **, represents that the test passed at a significance level of 0.01. DJF represents December and next January and February. MAM represents March, April, and May. JJA represents June, July, and August. SON represents September, October, and November.

796
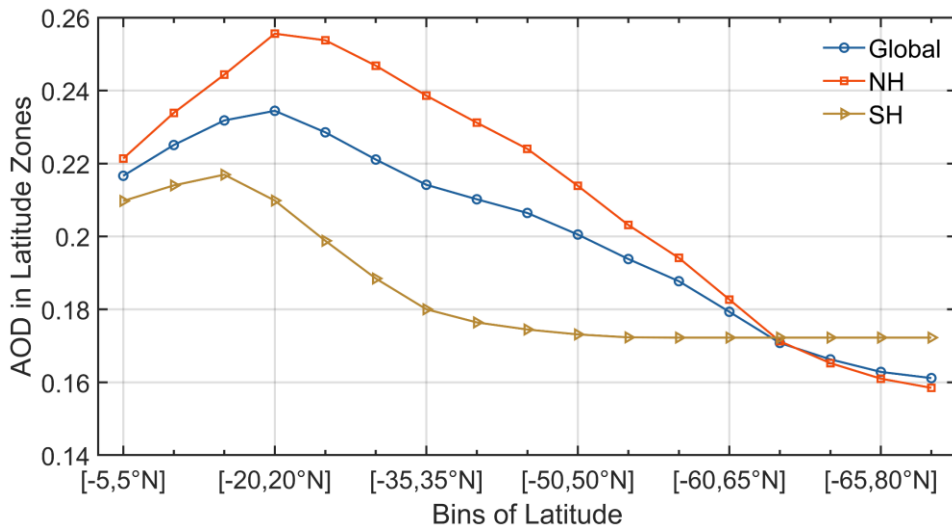
Figure 12 The global land (blue), northern hemisphere's (red) and southern hemisphere's (yellow) multi-year average VIS_AOD from 1980 to 2021 in different latitude zones. The latitude range is from -60 to 85°N, with a bin of 5°.**3.6 Interannual variability and trend of visibility-derived AOD over regions**

The distribution of AOD over global land exhibits significant spatial heterogeneity. Large variations in aerosol concentrations exist among different regions, leading to a non-uniform spatial distribution of AOD globally. Accurately assessing the long-term trends of aerosol loading is a key for quantifying aerosol climate change, and it is crucial for evaluating the effectiveness of measures implemented to improve regional air quality and reduce anthropogenic aerosol emissions.

To analyze the spatiotemporal characteristics and trends of AOD in different regions, we selected 12 representative regions that are influenced by various aerosol sources(Wang et al., 2009; Hsu et al., 2012; Chin et al., 2014), such as desert, industry, anthropogenic emissions, and biomass burning emissions, which nearly cover the most land and are densely populated regions (Kummu et al., 2016). These representative regions are Eastern Europe, Western Europe, Western North America, Eastern North America, Central South America, Western Africa, Southern Africa, Australia, Southeast Asia, Northeast Asia, Eastern China, and India, as shown in Figure 1. We use multi-year average and seasonal average AOD to evaluate aerosol loadings (Figure 13), the annual average of monthly anomalies to analyze interannual trends (Figure 14), and the seasonal average to analyze seasonal trends (Figure 15) in 12 regions from 1980 to 2021.

We can see some differences between VIS_AOD and MODIS AOD. In addition to model errors, the spatial matching between meteorological stations and MODIS, terrain, surface coverage, and station altitude will also bring errors. When particle transport and photochemical reactions occur above the boundary layer, visibility cannot capture the feature, which will also increase the uncertainty. However, bias is inevitable and can only be kept as small as possible. From the trend, they have similar changing characteristics, especially on monthly and yearly scales.

Figure 13 shows the regions with high AOD level from 1980 to 2021 (multi-year average AOD > 0.2) are in West Africa, Northeast Asia, Eastern China, and India. The AOD values in Eastern North America, Central South America, South Africa, and Southeast Asia range from 0.15 to 0.2. The AOD values in Eastern Europe, Western Europe, Western North America, and Australia are less than 0.15.

Europe is an industrial region with a low aerosol loading region, and the multi-year average AOD in Eastern Europe (0.144±0.007) is higher than that in Western Europe (0.139±0.003) during 1980-2021. Eastern Europe shows a greater downward trend in AOD (-0.0041/10a) compared to Western Europe (-0.0021/10a). The highest AOD is observed in JJA, the dry period when solar irradiation and boundary layer height increase, with Eastern Europe at 0.161 and Western Europe at 0.162, which could be due to increases in secondary aerosols, biomass burning, and dust transport from the Sahara (Mehta et al., 2016). However, there are seasonal variations. In Eastern Europe, the seasonal AOD ranking from high to low is JJA (0.161) > DJF (0.147) > MAM (0.138) > SON (0.131), while in Western Europe, it is JJA (0.162) > MAM (0.140) > SON (0.136) > DJF (0.117). The differences among seasons are larger in Western Europe. AOD in Eastern Europe shows declining trends in all seasons, while it does not pass the significance test in MAM. Among four seasons, SON has the largest decline trend of AOD (-0.0058/10a). In Western Europe, DJF, JJA, and

SON exhibit declining trends of AOD that pass the significance test, while the MAM shows a significant increase trend of AOD (0.0022/10a), which may be due to eruptions of the Eyjafjallajökull volcano in Iceland in spring 2010 (Karbowska and Zembrzuski, 2016). Both Western and Eastern Europe experienced increasing trends in AOD during the period of 1995-2005, with Western Europe showing a greater increase. However, after 2000, the decline rate accelerated in both regions. The downward trend in Europe is attributed to the reduction of biomass burning, anthropogenic aerosols, and aerosol precursors (such as sulfur dioxide)(Wang et al., 2009; Chin et al., 2014; Mortier et al., 2020).

North America is also an industrial region with a low aerosol loading. The average AOD values for Eastern and Western North America during 1980-2021 are 0.153±0.004 and 0.131±0.005, respectively, with the Eastern region being higher than the Western region by 0.022. From 1980 to 2021, both Eastern (-0.0021/10a) and Western North America (-0.0009/10a) show a downward trend; however, the decline in the Western region is not statistically significant. And the trend is -0.0172/10a from 1995 to 2005 and 0.0096/10a from 2005 to 2021.The average AOD values in DJF, MAM, JJA, and SON in Western North America are 0.1367, 0.1286, 0.1457, and 0.114, respectively, compared to 0.137, 0.145, 0.1913, and 0.138 in Eastern North America. The lowest AOD values of 12 regions during DJF and SON are observed in Western North America (Remer et al., 2008). Specifically, in the Western region, there is a consistent increasing trend during MAM (0.004/10a) from 1980 to 2021, while JJA and SON also show an increase after 2000, except for DJF (-0.0032/10a). In contrast, the AOD trends in the Eastern region remain unchanged during the period 1980-2021, except for MAM, which shows a stable increasing trend (0.0033/10a), while DJF, JJA, and SON exhibit decreasing trends (-0.0023/10a, -0.0040/10a, -0.0053/10a, respectively). In the Western region, the annual mean AOD started to increase after 2005, while in the Eastern region, the increase was not significant. The upward trend may be due to low rainfall and increased wildfire activities (Yoon et al., 2014). The decrease in AOD in Eastern North America is related to the reduction of sulfate and organic aerosols, as well as the decrease in anthropogenic emissions caused by environmental regulations (Mehta et al., 2016).

Central South America is a relatively high aerosol loading region, sourced from biomass burning, especially in SON (Remer et al., 2008; Mehta et al., 2016), with a multi-year average AOD of 0.192±0.017. There is a clear downward trend (-0.0100/10a) from 1980 to 2021, which is slightly greater than the trend (-0.0090/10a) from 1998 to 2010 (Hsu et al., 2012) and AOD decreased from 1980 to 2006 (Streets et al., 2009) and from 2001 to 2014 (Mehta et al., 2016). Although DJF (0.199) and SON (0.226) have higher values compared to MAM (0.180) and JJA (0.163), the large declining trends are observed in MAM (-0.0126/10a) and JJA (-0.0167/10a). It indicates that although AOD has decreased overall, the aerosol loading caused by seasonal deforestation and biomass combustion is still large(Mehta et al., 2016).

Africa is also one of the regions with a high aerosol loading worldwide. In West Africa, the average AOD is 0.275±0.012 during 1980-2021, and the annual AOD shows a downward trend (-0.0008/10a, p>0.05). The world's largest desert (Sahara Desert) is in West Africa, with much dust aerosol discharged. AOD values in all seasons are above 0.25, with JJA (0.301) and MAM (0.300) reaching 0.3, and DJF and SON being 0.252 and 0.250, respectively. The AOD in DJF (-0.0135/10a, p<0.01) and SON (-0.0026/10, p>0.05) exhibit decreasing trends, while JJA (0.0088/10a, p<0.01) and MAM (0.0037/10a, p>0.05) show an opposite trend. The multi-year average AOD in South Africa is

0.177±0.020, lower than that of West Africa. The annual mean AOD in South Africa shows a significant decrease (-0.0096/10a). The AOD values range from 0.12 to 0.2 during 2000-2009, dominated by fine particle matter from industrial pollution from biomass and fossil fuel combustion (Hersey et al., 2015). The average AOD values in DJF, MAM, JJA, and SON are 0.189, 0.162, 0.147, and 0.210, respectively. JJA (-0.0268/10a, $p<0.01$), MAM (-0.0126/10a, $p<0.01$) and SON (-0.0001/10a, $p>0.05$) exhibit a downward AOD trend, while DJF (0.0006/10a, $p>0.05$) shows an upward trend. AERONET and simulation results also show a decreasing trend of AOD (Chin et al., 2014).

Australia is a region with a low aerosol loading. The multi-year mean AOD is 0.127±0.014 during 1980-2021. The AOD ranges from 0.05 to 0.15 from AERONET during 2000-2021, and dust and biomass burning are important contributors to the aerosol loading (Yang et al., 2021a). There is a downward trend of AOD (-0.0081/10a, $p<0.01$), which may be related to a decrease in dust and biomass burning (Yoon et al., 2016; Yang et al., 2021a). In addition, research has shown that the forest area in Australia has increased sharply since 2000 (Giglio et al., 2013), surpassing the forest fire area of the past 14 years. The seasonal average of AOD in MAM, JJA, SON, and DJF are 0.122, 0.108, 0.125, and 0.151. The AOD in JJA is the lowest among all seasons and regions. The highest AOD is in DJF with an increasing trend (0.0056/10a, $p<0.01$), while the trends during MAM, JJA and SON are -0.0096/10a ($p<0.01$), -0.0231/10a ($p<0.01$) and -0.0042/10a ($p<0.01$), respectively. Ground-based and satellite observations indicate that wildfires, biomass burning and sandstorms lead to high AOD in DJF and SON. The low AOD of MAM and JJA is due to a decrease in the frequency of sandstorms and wildfires and an increase in precipitation (Gras et al., 1999; Yang et al., 2021a; Yang et al., 2021b).

Asia is also a high aerosol loading area with various sources. In Southeast Asia, the multi-year average AOD is 0.177 during 1980-2021 with a downward trend of AOD (-0.0003/10a, $p>0.05$). It is also a biomass-burning area. The seasonal average AOD ranking from high to low is JJA (0.207) > MAM (0.183) > DJF (0.169) > SON (0.149). The trends in DJF (-0.0035/10a, $p<0.05$), JJA (-0.0007/10a, $p>0.05$) and SON (-0.0021/10a, $p>0.05$) are opposite to MAM (0.0050/10a, $p<0.01$). Southeast Asia has no clear long-term trend in estimated AOD or observed surface solar radiation (Streets et al., 2009). In Northeast Asia, the multi-year average AOD is 0. 222 during 1980-2021, with no significant temporal trend. The seasonal AOD values are 0.252 in MAM, 0.215 in DJF, 0.212 in SON and 0.209 in JJA. AOD in MAM is significantly higher than other seasons, which may be related to sandstorms in East Asia, and the reason for the high AOD in winter may be related to the transportation. The trends of AOD in DJF (-0.0025/10a, $p>0.05$), MAM (0.0031/10a, $p>0.05$), JJA (0) and SON (-0.0006/10a, $p>0.05$) are not significant. In Eastern China, the multi-year average AOD is 0.233, with an increasing trend (0.0071/10a, $p<0.01$). The trend is 0.0151/10a from 1980 to 2006 and -0.0469/10a from 2006 to 2021.The seasonal average AOD ranking from high to low is JJA (0.284), MAM (0.234), SON (0.230) and DJF (0.183). The AOD trends in DJF (0.0093/10a, $p<0.01$), MAM (0.0092/10a, $p<0.01$), JJA (0.0038/10a, $p>0.05$) and SON (0.0065/10a, $p<0.05$) are all positive but the trend in JJA does not pass the significance test. We can see that there are three stages of changes in AOD: 1980-2005, 2006-2013 and 2014-2021. In the first stage, AOD increased steadily. In the second stage, AOD maintained a larger positive anomaly accompanied by oscillations. The third stage experienced a rapid decline, reaching the level of the 1980s by 2021. The increasing trend of AOD before 2006 may be due to the significant increase in industrial activity,

and after 2013, the significant decrease is closely related to the implementation of air quality-related laws and regulations, along with adjustments in the energy structure (Hu et al., 2018; Cherian and Quaas, 2020).

India is a high aerosol loading area. The multi-year average AOD is 0.255, with an upward trend (0.0096/10a, p<0.01) from 1980 to 2021. Dust and biomass burning has an influence on AOD level. There are three stages: 1980-1997 (0.0032/10a, p<0.01), 1997-2005 (-0.0420/10a, p<0.01), 2005-2021 (0.0481/10a, p<0.01). Although the trend is downward in the second stage, the lager positive trend is in the third stage. The seasonal average AOD values are 0.237 in DJF, 0.258 in MAM, 0.269 in JJA, and 0.256 in SON. The largest AOD is in JJA. In winter and autumn, it affected by biomass burning, and in spring and summer, it is also affected by dust, transported from the Sahara under during the monsoon period (Remer et al., 2008). The trends in DJF (0.0152/10a, p<0.01), MAM (0.0091/10a, p<0.01), JJA (0.0025/10a, p>0.05), and SON (0.0107/10a, p<0.05) are positive. There largest trend is in winter.

To summarize, there are significant differences in the spatial distribution, annual trends, and seasonal trends of AOD across different regions from 1980 to 2021. The high aerosol loadings from 1980 to 2021 are in West Africa, India and Asia, and low aerosol loading regions are in Europe, Western North America, and Australia. Eastern China and India show an increasing trend, Southeast Asia and Northeast Asia show no significant trend, and the other regions show downward trends. However, not all regional seasonal trends are consistent with their annual trends. The results in this study have supplemented the long-term trend and distribution of AOD over land.
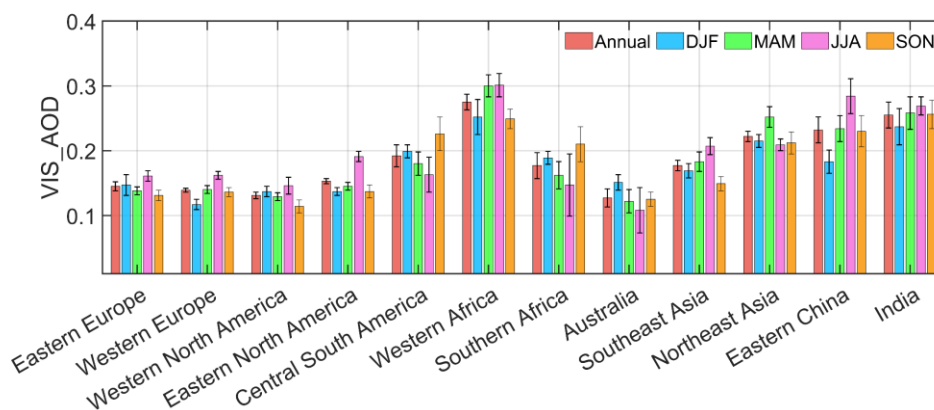
Figure 13 Annual and seasonal averages of AOD in 12 regions during 1980-2021.

948
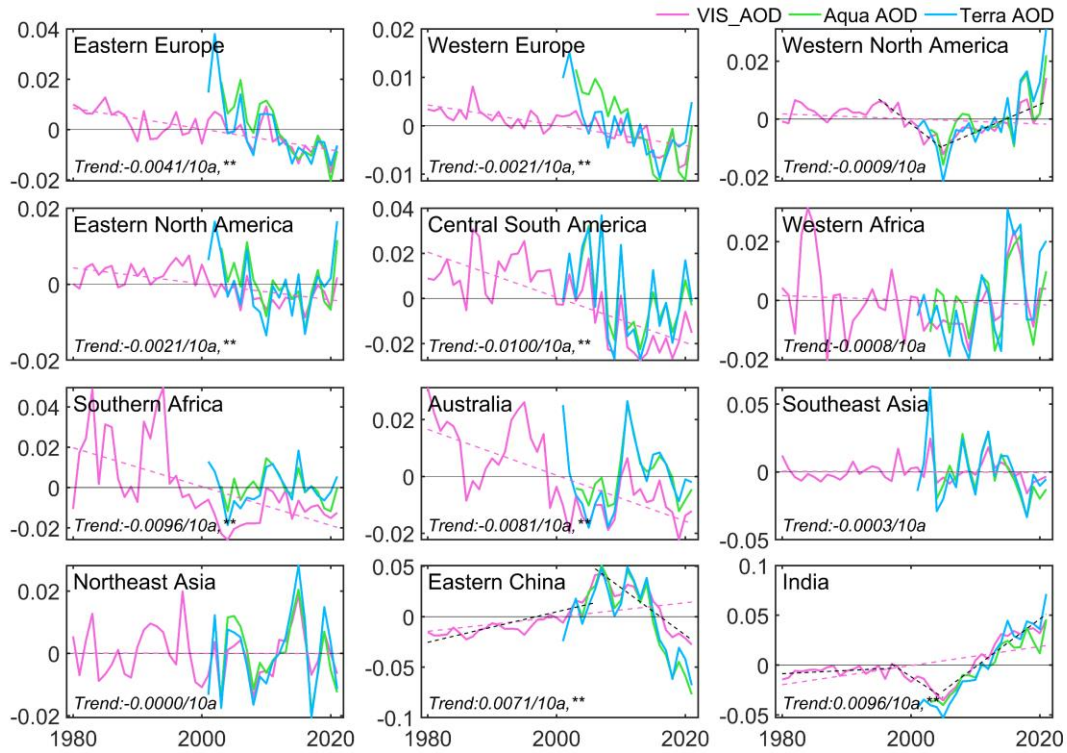
Figure 14 Annual averages of monthly anomaly gridded VIS_AOD (pink line), Aqua (green line), and Terra (blue line) MODIS AOD in 12 regions. The dotted line is the trend line.

951

952
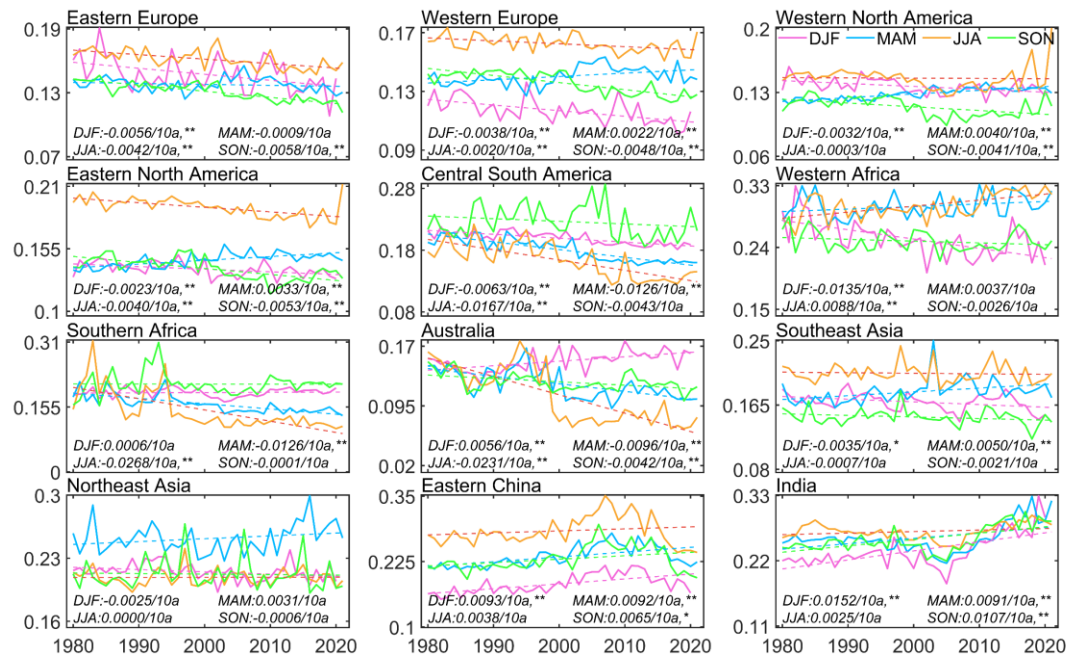
Figure 15 Seasonal averages of gridded VIS_AOD during 1980 to 2021 in 12 regions (Eastern Europe, Western Europe, Western North America, Eastern North America, Central South America, Western Africa, Southern Africa, Australia, Southeast Asia, Northeast Asia, Eastern China, and

India). The dotted line is the trend line.

4 Data availability

The visibility-derived AOD at station and grid scales over global land from 1980 to 2021 are available at National Tibetan Plateau / Third Pole Environment Data Center (https://doi.org/10.11888/Atmos.tpdc.300822) (Hao et al., 2023).

5 Conclusions

In this study, we employed a machine learning technique to derive AOD for over 5000 land stations worldwide, based on satellite data, visibility, and related parameters. Monthly AOD was interpolated onto a 0.5° grid using ordinary kriging with area weighting. The method was trained with Aqua MODIS AOD. The accuracy and performance of the derived AOD were assessed and validated against Terra MODIS AOD as well as AERONET ground-based observations of AOD for the corresponding stations. Evaluation of the gridded AOD was conducted using Aqua and Terra MODIS AOD. We obtained daily AOD for global land stations from 1980 to 2021, as well as monthly gridded AOD. The two datasets complement the shortcomings of AOD in terms of time scale and spatial coverage. Finally, the spatiotemporal variation in AOD was analyzed for global land, the Southern Hemisphere, the Northern Hemisphere, and 12 regions in the past 42 years. Several key findings have been obtained in this study as follows.

1. Modeling and gridding evaluation. The mean RMSE, MAE, and R of all stations are 0.078, 0.044, and 0.750, respectively. The RMSE of 93% stations is less than 0.11, the MAE of 91% is less than 0.06, and the R of 88% is greater than 0.7, respectively. Compared to Aqua and Terra, the average biases of gridded AOD are 3.3% and 1.9%, and the spatial correlation coefficients are 0.80 and 0.79, with the zonal correlation coefficients of 0.99 and 0.99 and the meridional correlation coefficients of 0.99 and 0.90.

2. Model validation. For the daily scale, the R, RMSE and MAE of between VIS_AOD and Aqua AOD is 0.799, 0.079 and 0.044, respectively. The percentage of sample point falling within the EE envelopes is 84.12%. The R between VIS_AOD and Terra AOD is 0.542, with a RMSE of 0.125 and MAE of 0.078. The percentage falling within the EE envelopes is 64.76%. The R between VIS_AOD and AERONET AOD is 0.546, with a RMSE of 0.186 and MAE of 0.099. The percentage falling within the EE envelopes is 57.87%. For the monthly and annual scales, RMSE and MAE show a significant decrease between VIS_AOD and Aqua, Terra, and AERONET AOD, and R and percentages falling within EE show a significant increase.

3. Error analysis. The average bias is 0.015 (AOD <0.1), with 83% of data within the EE envelopes. As pollution level increases, the negative mean bias becomes significant and the underestimation increases. There is a negative bias in the low elevation (<=0.5km) with a percentage of 60%-64% falling within the EE envelopes and a positive bias in high elevation (0.5-1.2km) with a percentage of 50%-65% falling within the EE envelopes. The elevation of AERONET's site caused a bias in high elevation. When the elevation difference is negative (the elevation of the meteorological station is lower than that of the AERONET site), there is a significant positive bias. When the difference is

positive, the mean bias approaches 0 or is positive. The bias does not change significantly with increasing distance between the meteorological station and AERONET site.

4. Global land AOD. The global, NH, and SH AOD values from 1980 to 2021 are 0.161 ± 0.074, 0.158 ± 0.076, and 0.173 ± 0.059, respectively. Trends in AOD for the global, NH, and SH demonstrate a decreasing trend of -0.0026/10a, -0.0018/10a, and -0.0059/10a, respectively ($p<0.01$). The seasonal AOD ranking from high to low is JJA>MAM>DJF>SON over the global land and in the NH, while in the SH, it is DJF>JJA>MAM>SON. The largest declining trends are observed in NH summer and SH winter.

4. Regional AOD. From 1980 to 2021, regions with high aerosol loadings (AOD > 0.2) were found in West Africa, Northeast Asia, Eastern China, and India. Regions with moderate aerosol loadings (AOD between 0.15 and 0.2) are Eastern North America, Central South America, South Africa, and Southeast Asia. Eastern Europe, Western Europe, Western North America, and Australia are regions with low aerosol loadings (AOD < 0.15). The trends are -0.0041/10a, -0.0021/10a, -0.0009/10a, -0.0021/10a, -0.0100/10a, -0.0008/10a, -0.0096/10a), -0.0081/10a, -0.0003/10a, -0.0000/10a, 0.0071/10a, and 0.0096/10a in Eastern Europe, Western Europe, Western North America, Eastern North America, Central South America, Western Africa, Southern Africa, Australia, Southeast Asia, Northeast Asia, Eastern China, and India, respectively.

Competing interests

The contact author has declared that none of the authors has any competing interests.

Acknowledgments

This work was supported by the National Key Research & Development Program of China (2022YFF0801302) and the National Natural Science Foundation of China (41930970). The hourly visibility data were download from https://mesonet.agron.iastate.edu/ASOS. The Aerosol Robotic Network (AERONET) 15-minute aerosol optical depth (AOD) data were download from which can be downloaded from https://aeronet.gsfc.nasa.gov. The MODIS AOD data were download from https://ladsweb.modaps.eosdis.nasa.gov.

References

Ackerman, A. S., Hobbs, P. V., and Toon, O. B.: A model for particle microphysics, turbulent mixing, and radiative transfer in the stratocumulus-topped marine boundary layer and comparisons with measurements, J. Atmos. Sci., 52, 1204-1236, https://doi.org/10.1175/1520-0469(1995)052<1204:AMFPMT>2.0.CO;2, 1995.

Albrecht, B. A.: Aerosols, cloud microphysics, and fractional cloudiness, Science, 245, 1227-1230, 1989.

Anderson, T. L., Charlson, R. J., Bellouin, N., Boucher, O., Chin, M., Christopher, S. A., Haywood, J., Kaufman, Y. J., Kinne, S., Ogren, J. A., Remer, L. A., Takemura, T., Tanre, D., Torres, O., Trepte, C. R., Wielicki, B. A., Winker, D. M., and Yu, H. B.: An "A-Train" strategy for quantifying direct climate forcing by anthropogenic aerosols, B. Am. Meteorol. Soc., 86, 1795-+, https://doi.org/10.1175/Bams-86-

12-1795, 2005.

Andersson, S. M., Martinsson, B. G., Vernier, J.-P., Friberg, J., Brenninkmeijer, C. A., Hermann, M., Van Velthoven, P. F., and Zahn, A.: Significant radiative impact of volcanic aerosol in the lowermost stratosphere, Nat. Commun., 6, 7692, https://doi.org/10.1038/ncomms8692, 2015.

Andrews, E., Sheridan, P. J., Ogren, J. A., Hageman, D., Jefferson, A., Wendell, J., Alástuey, A., Alados-Arboledas, L., Bergin, M., and Ealo, M.: Overview of the NOAA/ESRL federated aerosol network, B. Am. Meteorol. Soc., 100, 123-135, https://doi.org/10.1175/BAMS-D-17-0175.1, 2019.

Bergstrom, R. W., Pilewskie, P., Russell, P. B., Redemann, J., Bond, T. C., Quinn, P. K., and Sierau, B.: Spectral absorption properties of atmospheric aerosols, Atmos. Chem. Phys., 7, 5937-5943, https://doi.org/10.5194/acp-7-5937-2007, 2007.

Bescond, A., Yon, J., Girasole, T., Jouen, C., Rozé, C., and Coppalle, A.: Numerical investigation of the possibility to determine the primary particle size of fractal aggregates by measuring light depolarization, J. Quant. Spectrosc. Ra., 126, 130-139, https://doi.org/10.1016/j.jqsrt.2012.10.011, 2013.

Boers, R., van Weele, M., van Meijgaard, E., Savenije, M., Siebesma, A. P., Bosveld, F., and Stammes, P.: Observations and projections of visibility and aerosol optical thickness (1956-2100) in the Netherlands: impacts of time-varying aerosol composition and hygroscopicity, Environ. Res. Lett., 10, https://doi.org/10.1088/1748-9326/10/1/015003, 2015.

Bokoye, A. I., Royer, A., O'Neil, N., Cliche, P., Fedosejevs, G., Teillet, P., and McArthur, L.: Characterization of atmospheric aerosols across Canada from a ground-based sunphotometer network: AEROCAN, Atmos. Ocean, 39, 429-456, https://doi.org/10.1080/07055900.2001.9649687, 2001.

Bösenberg, J. and Matthias, V.: EARLINET: A European Aerosol Research Lidar Network to Establish an Aerosol Climatology, Max Planck Institut Fur Meteorologie, 2003.

Bright, J. M. and Gueymard, C. A.: Climate-specific and global validation of MODIS Aqua and Terra aerosol optical depth at 452 AERONET stations, Sol. Energy, 183, 594-605, https://doi.org/10.1016/j.solener.2019.03.043, 2019.

Browne, M. W.: Cross-validation methods, J. Math. Psychol., 44, 108-132, https://doi.org/10.1006/jmps.1999.1279, 2000.

Calvo, A. I., Alves, C., Castro, A., Pont, V., Vicente, A. M., and Fraile, R.: Research on aerosol sources and chemical composition: Past, current and emerging issues, Atmos. Res., 120, 1-28, https://doi.org/10.1016/j.atmosres.2012.09.021, 2013.

Chafe, Z. A., Brauer, M., Klimont, Z., Van Dingenen, R., Mehta, S., Rao, S., Riahi, K., Dentener, F., and Smith, K. R.: Household Cooking with Solid Fuels Contributes to Ambient PM2.5 Air Pollution and the Burden of Disease, Environ. Health Persp., 122, 1314-1320, https://doi.org/10.1289/ehp.1206340, 2014.

Chazette, P., David, C., Lefrère, J., Godin, S., Pelon, J., and Mégie, G.: Comparative lidar study of the optical, geometrical, and dynamical properties of stratospheric post-volcanic aerosols, following the eruptions of El Chichon and Mount Pinatubo, J. Geophys. Res-Atmos., 100, 23195-23207, https://doi.org/10.1029/95JD02268, 1995.

Che, H., Zhang, X., Chen, H., Damiri, B., Goloub, P., Li, Z., Zhang, X., Wei, Y., Zhou, H., Dong, F., Li, D., and Zhou, T.: Instrument calibration and aerosol optical depth validation of the China Aerosol Remote Sensing Network, J. Geophys. Res-Atmos., 114, https://doi.org/10.1029/2008jd011030, 2009.

Che, H., Xia, X., Zhu, J., Li, Z., Dubovik, O., Holben, B., Goloub, P., Chen, H., Estelles, V., Cuevas-Agullo, E., Blarel, L., Wang, H., Zhao, H., Zhang, X., Wang, Y., Sun, J., Tao, R., Zhang, X., and Shi, G.: Column aerosol optical properties and aerosol radiative forcing during a serious haze-fog month over North China Plain in 2013 based on ground-based sunphotometer measurements, Atmos. Chem. Phys.,

14, 2125-2138, https://doi.org/10.5194/acp-14-2125-2014, 2014.

Chen, A., Zhao, C., and Fan, T.: Spatio-temporal distribution of aerosol direct radiative forcing over mid-latitude regions in north hemisphere estimated from satellite observations, Atmos. Res., 266, 105938, https://doi.org/10.1016/j.atmosres.2021.105938, 2022.

Chen, D., Ou, T., Gong, L., Xu, C.-Y., Li, W., Ho, C.-H., and Qian, W.: Spatial Interpolation of Daily Precipitation in China: 1951-2005, Adv. Atmos. Sci., 27, 1221-1232, https://doi.org/10.1007/s00376-010-9151-y, 2010.

Cherian, R. and Quaas, J.: Trends in AOD, clouds, and cloud radiative effects in satellite data and CMIP5 and CMIP6 model simulations over aerosol source regions, Geophys. Res. Lett., 47, e2020GL087132, https://doi.org/10.1029/2020GL087132, 2020.

Chin, M., Diehl, T., Tan, Q., Prospero, J., Kahn, R., Remer, L., Yu, H., Sayer, A., Bian, H., and Geogdzhayev, I.: Multi-decadal aerosol variations from 1980 to 2009: a perspective from observations and a global model, Atmos. Chem. Phys., 14, 3657-3690, https://doi.org/10.5194/acp-14-3657-2014, 2014.

Chu, D., Kaufman, Y., Ichoku, C., Remer, L., Tanré, D., and Holben, B.: Validation of MODIS aerosol optical depth retrieval over land, Geophys. Res. Lett., 29, MOD2-1-MOD2-4, https://doi.org/10.1029/2001GL013205, 2002.

Chuang, P.-J. and Huang, P.-Y.: B-VAE: a new dataset balancing approach using batched Variational AutoEncoders to enhance network intrusion detection, J. Supercomput., https://doi.org/10.1007/s11227-023-05171-w, 2023.

Deuzé, J., Goloub, P., Herman, M., Marchand, A., Perry, G., Susana, S., and Tanré, D.: Estimate of the aerosol properties over the ocean with POLDER, J. Geophys. Res-Atmos., 105, 15329-15346, https://doi.org/10.1029/2000JD900148, 2000.

Dhanya, R., Paul, I. R., Akula, S. S., Sivakumar, M., and Nair, J. J.: F-test feature selection in Stacking ensemble model for breast cancer prediction, Procedia. Comput. Sci., 171, 1561-1570, https://doi.org/10.1016/j.procs.2020.04.167, 2020.

Diner, D. J., Beckert, J. C., Reilly, T. H., Bruegge, C. J., Conel, J. E., Kahn, R. A., Martonchik, J. V., Ackerman, T. P., Davies, R., and Gerstl, S. A. W.: Multi-angle Imaging SpectroRadiometer (MISR) instrument description and experiment overview, Ieee T. Geosci. Remote., 98, 1072-1087, https://doi.org/10.1109/36.700992, 1998.

Dong, Y., Li, J., Yan, X., Li, C., Jiang, Z., Xiong, C., Chang, L., Zhang, L., Ying, T., and Zhang, Z.: Retrieval of aerosol single scattering albedo using joint satellite and surface visibility measurements, Remote Sens. Environ., 294, 113654, https://doi.org/10.1016/j.rse.2023.113654, 2023.

Dubovik, Oleg, Holben, Brent, Eck, Thomas, F., Smirnov, Alexander, and Kaufman: Variability of Absorption and Optical Properties of Key Aerosol Types Observed in Worldwide Locations, J. Atmos. Sci., 59, 590-590, https://doi.org/10.1175/1520-0469(2002)059<0590:VOAAOP>2.0.CO;2, 2002a.

Dubovik, O., Smirnov, A., Holben, B. N., King, M. D., Kaufman, Y. J., Eck, T. F., and Slutsker, I.: Accuracy assessments of aerosol optical properties retrieved from Aerosol Robotic Network (AERONET) Sun and sky radiance measurements, J. Geophys. Res-Atmos., 105, 9791-9806, https://doi.org/10.1029/2000jd900040, 2000.

Dubovik, O., Holben, B., Eck, T. F., Smirnov, A., Kaufman, Y. J., King, M. D., Tanré, D., and Slutsker, I.: Variability of absorption and optical properties of key aerosol types observed in worldwide locations, J. Atmos. Sci., 59, 590-608, https://doi.org/10.1175/1520-0469(2002)059<0590:VOAAOP>2.0.CO;2, 2002b.

Eck, T. F., Holben, B. N., Reid, J. S., Sinyuk, A., Giles, D. M., Arola, A., Slutsker, I., Schafer, J. S., Sorokin, M. G., and Smirnov, A.: The extreme forest fires in California/Oregon in 2020: Aerosol optical and physical properties and comparisons of aged versus fresh smoke, Atmos. Environ., 305, 119798, https://doi.org/10.1016/j.atmosenv.2023.119798, 2023.

Elterman, L.: Relationships between vertical attenuation and surface meteorological range, Appl. Optics, 9, 1804-1810, https://doi.org/10.1364/AO.9.001804, 1970.

Fan, H., Zhao, C., Yang, Y., and Yang, X.: Spatio-Temporal Variations of the $PM_{2.5}/PM_{10}$ Ratios and Its Application to Air Pollution Type Classification in China, Front. Environ. Sci., 9, https://doi.org/10.3389/fenvs.2021.692440, 2021.

Fernández, A., Garcia, S., Herrera, F., and Chawla, N. V.: SMOTE for learning from imbalanced data: progress and challenges, marking the 15-year anniversary, J. Artif. Intell. Res., 61, 863-905, https://doi.org/10.1613/jair.1.11192, 2018.

Forster, P., Ramaswamy, V., Artaxo, P., Berntsen, T., Betts, R., Fahey, D. W., Haywood, J., Lean, J., Lowe, D. C., and Myhre, G.: Changes in atmospheric constituents and in radiative forcing, Climate Change 2007: The Physical Science Basis. Contribution of Working Group I to the 4th Assessment Report of the Intergovernmental Panel on Climate Change, 2007.

Giglio, L., Randerson, J. T., and Van Der Werf, G. R.: Analysis of daily, monthly, and annual burned area using the fourth‐generation global fire emissions database (GFED4), J. Geophys. Res-Biogeo., 118, 317-328, https://doi.org/10.1002/jgrg.20042, 2013.

Giles, D. M., Sinyuk, A., Sorokin, M. G., Schafer, J. S., Smirnov, A., Slutsker, I., Eck, T. F., Holben, B. N., Lewis, J. R., Campbell, J. R., Welton, E. J., Korkin, S. V., and Lyapustin, A. I.: Advancements in the Aerosol Robotic Network (AERONET) Version 3 database – automated near-real-time quality control algorithm with improved cloud screening for Sun photometer aerosol optical depth (AOD) measurements, Atmos. Meas. Tech., 12, 169-209, https://doi.org/10.5194/amt-12-169-2019, 2019.

Goovaerts, P.: Geostatistical approaches for incorporating elevation into the spatial interpolation of rainfall, Journal of Hydrology, 228, 113-129, https://doi.org/10.1016/s0022-1694(00)00144-x, 2000.

Gras, J., Jensen, J., Okada, K., Ikegami, M., Zaizen, Y., and Makino, Y.: Some optical properties of smoke aerosol in Indonesia and tropical Australia, Geophys. Res. Lett., 26, 1393-1396, https://doi.org/10.1029/1999GL900275, 1999.

Guerrero-Rascado, J. L., Landulfo, E., Antuña, J. C., Barbosa, H. d. M. J., Barja, B., Bastidas, Á. E., Bedoya, A. E., da Costa, R. F., Estevan, R., and Forno, R.: Latin American Lidar Network (LALINET) for aerosol research: Diagnosis on network instrumentation, J. Atmos. Sol-Terr. Phy., 138, 112-120, https://doi.org/10.1016/j.jastp.2016.01.001, 2016.

Guo, J., Zhang, J., Yang, K., Liao, H., Zhang, S., Huang, K., Lv, Y., Shao, J., Yu, T., and Tong, B.: Investigation of near-global daytime boundary layer height using high-resolution radiosondes: first results and comparison with ERA5, MERRA-2, JRA-55, and NCEP-2 reanalyses, Atmos. Chem. Phys., 21, 17079-17097, https://doi.org/10.5194/acp-21-17079-2021, 2021.

Hao, H., Wang, K., and Wu, G.: Visibility-derived aerosol optical depth over global land (1980-2021), National Tibetan Plateau Data Center [dataset], https://doi.org/10.11888/Atmos.tpdc.300822, 2023.

He, H., Bai, Y., Garcia, E. A., and Li, S.: ADASYN: Adaptive synthetic sampling approach for imbalanced learning, IEEE World Congress on Computational Intelligence, 1322-1328, https://doi.org/10.1109/IJCNN.2008.4633969, 2008.

Hersbach, H., Bell, B., Berrisford, P., Hirahara, S., Horányi, A., Muñoz‐Sabater, J., Nicolas, J., Peubey, C., Radu, R., and Schepers, D.: The ERA5 global reanalysis, Q. J. Roy. Meteor. Soc., 146, 1999-2049,

https://doi.org/10.1002/qj.3803, 2020.

Hersey, S. P., Garland, R. M., Crosbie, E., Shingler, T., Sorooshian, A., Piketh, S., and Burger, R.: An overview of regional and local characteristics of aerosols in South Africa using satellite, ground, and modeling data, Atmos. Chem. Phys., 15, 4259-4278, https://doi.org/10.5194/acp-15-4259-2015, 2015.

Hirono, M. and Shibata, T.: Enormous increase of stratospheric aerosols over Fukuoka due to volcanic eruption of El Chichon in 1982, Geophys. Res. Lett., 10, 152-154, https://doi.org/10.1029/GL010i002p00152, 1983.

Hofmann, D., Barnes, J., O'Neill, M., Trudeau, M., and Neely, R.: Increase in background stratospheric aerosol observed with lidar at Mauna Loa Observatory and Boulder, Colorado, Geophys. Res. Lett., 36, https://doi.org/10.1029/2009GL039008, 2009.

Holben, B. N., Eck, T. F., Slutsker, I., Tanre, D., Buis, J. P., Setzer, A., Vermote, E., Reagan, J. A., Kaufman, Y. J., Nakajima, T., Lavenu, F., Jankowiak, I., and Smirnov, A.: AERONET - A federated instrument network and data archive for aerosol characterization, Remote Sens. Environ., 66, 1-16, https://doi.org/10.1016/s0034-4257(98)00031-5, 1998.

Hsu, N., Gautam, R., Sayer, A., Bettenhausen, C., Li, C., Jeong, M., Tsay, S.-C., and Holben, B.: Global and regional trends of aerosol optical depth over land and ocean using SeaWiFS measurements from 1997 to 2010, Atmos. Chem. Phys., 12, 8037-8053, https://doi.org/10.5194/acp-12-8037-2012, 2012.

Hsu, N., Jeong, M. J., Bettenhausen, C., Sayer, A., Hansell, R., Seftor, C., Huang, J., and Tsay, S. C.: Enhanced Deep Blue aerosol retrieval algorithm: The second generation, J. Geophys. Res-Atmos., 118, 9296-9315, https://doi.org/10.1002/jgrd.50712, 2013.

Hsu, N., Lee, J., Sayer, A., Carletta, N., Chen, S. H., Tucker, C., Holben, B., and Tsay, S. C.: Retrieving near-global aerosol loading over land and ocean from AVHRR, J. Geophys. Res-Atmos., 122, 9968-9989, https://doi.org/10.1002/2017JD026932, 2017.

Hsu, N. C., Tsay, S.-C., King, M. D., and Herman, J. R.: Deep blue retrievals of Asian aerosol properties during ACE-Asia, Ieee T. Geosci. Remote., 44, 3180-3195, https://doi.org/10.1109/tgrs.2006.879540, 2006.

Hu, B., Zhang, X., Sun, R., and Zhu, X.: Retrieval of Horizontal Visibility Using MODIS Data: A Deep Learning Approach, Atmosphere-Basel, 10, https://doi.org/10.3390/atmos10120740, 2019.

Hu, K., Kumar, K. R., Kang, N., Boiyo, R., and Wu, J.: Spatiotemporal characteristics of aerosols and their trends over mainland China with the recent Collection 6 MODIS and OMI satellite datasets, Environ. Sci. Pollut. R., 25, 6909-6927, https://doi.org/10.1007/s11356-017-0715-6, 2018.

Husar, R. B., Husar, J. D., and Martin, L.: Distribution of continental surface aerosol extinction based on visual range data, Atmos. Environ., 34, 5067-5078, https://doi.org/10.1016/s1352-2310(00)00324-1, 2000.

IPCC: Climate Change 2021: The Physical Science Basis, Cambridge University Press, New York, 2021.

Ivanova, G., Ivanov, V., Kukavskaya, E., and Soja, A.: The frequency of forest fires in Scots pine stands of Tuva, Russia, Environ. Res. Lett., 5, 015002, https://doi.org/10.1088/1748-9326/5/1/015002, 2010.

Kang, Y., Kim, M., Kang, E., Cho, D., and Im, J.: Improved retrievals of aerosol optical depth and fine mode fraction from GOCI geostationary satellite data using machine learning over East Asia, Isprs J. Photogramm., 183, 253-268, https://doi.org/10.1016/j.isprsjprs.2021.11.016, 2022.

Kang, Y., Choi, H., Im, J., Park, S., Shin, M., Song, C.-K., and Kim, S.: Estimation of surface-level NO2 and O3 concentrations using TROPOMI data and machine learning over East Asia, Environ. Pollut., 288, 117711, https://doi.org/10.1016/j.envpol.2021.117711, 2021.

Karbowska, B. and Zembrzuski, W.: Fractionation and mobility of thallium in volcanic ashes after

eruption of Eyjafjallajökull (2010) in Iceland, B. Environ. Contam. Tox., 97, 37-43, https://doi.org/10.1007/s00128-016-1831-6, 2016.

Kaufman, Y. J. and Boucher, O.: A satellite view of aerosols in the climate system, Nature, 419, 215-215, https://doi.org/10.1038/nature01091, 2002.

Kim, D. H., Sohn, B. J., Nakajima, T., Takamura, T., Takemura, T., Choi, B. C., and Yoon, S. C.: Aerosol optical properties over east Asia determined from ground-based sky radiation measurements, J. Geophys. Res-Atmos., 109, https://doi.org/10.1029/2003jd003387, 2004.

Klett, J. D.: Lidar inversion with variable backscatter/extinction ratios, Appl. Optics, 24, 1638-1643, https://doi.org/10.1364/AO.24.001638, 1985.

Koelemeijer, R., Homan, C., and Matthijsen, J.: Comparison of spatial and temporal variations of aerosol optical thickness and particulate matter over Europe, Atmos. Environ., 40, 5304-5315, https://doi.org/10.1016/j.atmosenv.2006.04.044, 2006.

Koschmieder, H.: Theorie der horizontalen Sichtweite, Beitrage zur Physik der freien Atmosphare, 12, 33-55, 1924.

Krylov, A., McCarty, J. L., Potapov, P., Loboda, T., Tyukavina, A., Turubanova, S., and Hansen, M. C.: Remote sensing estimates of stand-replacement fires in Russia, 2002–2011, Environ. Res. Lett., 9, 105007, https://doi.org/10.1088/1748-9326/9/10/105007, 2014.

Kulmala, M., Vehkamäki, H., Petäjä, T., Dal Maso, M., Lauri, A., Kerminen, V. M., Birmili, W., and McMurry, P. H.: Formation and growth rates of ultrafine atmospheric particles: A review of observations, J. Aerosol Sci., 35, 143-176, https://doi.org/10.1016/j.jaerosci.2003.10.003, 2004.

Kummu, M., De Moel, H., Salvucci, G., Viviroli, D., Ward, P. J., and Varis, O.: Over the hills and further away from coast: global geospatial patterns of human and environment over the 20th–21st centuries, Environ. Res. Lett., 11, 034010, https://doi.org/10.1088/1748-9326/11/3/034010, 2016.

Lapen, D. R. and Hayhoe, H. N.: Spatial analysis of seasonal and annual temperature and precipitation normals in southern Ontario, Canada, J. Great Lakes Res., 29, 529-544, https://doi.org/10.1016/s0380-1330(03)70457-2, 2003.

Lee, L. A., Reddington, C. L., and Carslaw, K. S.: On the relationship between aerosol model uncertainty and radiative forcing uncertainty, P. Natl. A. Sci., 113, 5820-5827, https://doi.org/10.1073/pnas.1507050113, 2016.

Levy, R. C., Remer, L. A., Mattoo, S., Vermote, E. F., and Kaufman, Y. J.: Second‐generation operational algorithm: Retrieval of aerosol properties over land from inversion of Moderate Resolution Imaging Spectroradiometer spectral reflectance, J. Geophys. Res-Atmos., 112, https://doi.org/10.1029/2006JD007811, 2007.

Levy, R. C., Mattoo, S., Munchak, L. A., Remer, L. A., Sayer, A. M., Patadia, F., and Hsu, N. C.: The Collection 6 MODIS aerosol products over land and ocean, Atmos. Meas. Tech., 6, 2989-3034, https://doi.org/10.5194/amt-6-2989-2013, 2013.

Levy, R. C., Mattoo, S., Sawyer, V., Shi, Y., Colarco, P. R., Lyapustin, A. I., Wang, Y., and Remer, L. A.: Exploring systematic offsets between aerosol products from the two MODIS sensors, Atmos. Meas. Tech., 11, 4073-4092, https://doi.org/10.5194/amt-11-4073-2018, 2018.

Li, J., Garshick, E., Hart, J. E., Li, L., Shi, L., Al-Hemoud, A., Huang, S., and Koutrakis, P.: Estimation of ambient PM2.5 in Iraq and Kuwait from 2001 to 2018 using machine learning and remote sensing, Environ. Int., 151, https://doi.org/10.1016/j.envint.2021.106445, 2021.

Li, J., Carlson, B. E., Yung, Y. L., Lv, D., Hansen, J., Penner, J. E., Liao, H., Ramaswamy, V., Kahn, R. A., Zhang, P., Dubovik, O., Ding, A., Lacis, A. A., Zhang, L., and Dong, Y.: Scattering and absorbing

aerosols in the climate system, Nat. Rev. Earth. Environ., 3, 363-379, https://doi.org/10.1038/s43017-022-00296-7, 2022.

Li, S., Chen, L., Huang, G., Lin, J., Yan, Y., Ni, R., Huo, Y., Wang, J., Liu, M., and Weng, H.: Retrieval of surface PM2. 5 mass concentrations over North China using visibility measurements and GEOS-Chem simulations, Atmos. Environ., 222, 117121, https://doi.org/10.1016/j.atmosenv.2019.117121, 2020.

Li, Z., Lau, W. M., Ramanathan, V., Wu, G., Ding, Y., Manoj, M., Liu, J., Qian, Y., Li, J., and Zhou, T.: Aerosol and monsoon climate interactions over Asia, Rev. Geophys., 54, 866-929, https://doi.org/10.1002/2015RG000500, 2016.

Liao, H., Chang, W., and Yang, Y.: Climatic Effects of Air Pollutants over China: A Review, Adv. Atmos. Sci., 32, 115-139, https://doi.org/10.1007/s00376-014-0013-x, 2015.

Lin, J. T., van Donkelaar, A., Xin, J. Y., Che, H. Z., and Wang, Y. S.: Clear-sky aerosol optical depth over East China estimated from visibility measurements and chemical transport modeling, Atmos. Environ., 95, 258-267, https://doi.org/10.1016/j.atmosenv.2014.06.044, 2014.

Liu, B., Ma, X., Ma, Y., Li, H., Jin, S., Fan, R., and Gong, W.: The relationship between atmospheric boundary layer and temperature inversion layer and their aerosol capture capabilities, Atmos. Res., 271, https://doi.org/10.1016/j.atmosres.2022.106121, 2022.

Mahowald, N. M., Ballantine, J. A., Feddema, J., and Ramankutty, N.: Global trends in visibility: implications for dust sources, Atmos. Chem. Phys., 7, 3309-3339, https://doi.org/10.5194/acp-7-3309-2007, 2007.

McNeill, V. F.: Atmospheric Aerosols: Clouds, Chemistry, and Climate, in: Annu. Rev. Chem. Biomol., edited by: Prausnitz, J. M., Annual Review of Chemical and Biomolecular Engineering, 427-444, https://doi.org/10.1146/annurev-chembioeng-060816-101538, 2017.

Mehta, M., Singh, R., Singh, A., and Singh, N.: Recent global aerosol optical depth variations and trends—A comparative study using MODIS and MISR level 3 datasets, Remote Sens. Environ., 181, 137-150, https://doi.org/10.1016/j.rse.2016.04.004, 2016.

Mitra, R., Bajpai, A., and Biswas, K.: ADASYN-assisted machine learning for phase prediction of high entropy carbides, Comp. Mater. Sci., 223, https://doi.org/10.1016/j.commatsci.2023.112142, 2023.

Mortier, A., Gliß, J., Schulz, M., Aas, W., Andrews, E., Bian, H., Chin, M., Ginoux, P., Hand, J., and Holben, B.: Evaluation of climate model aerosol trends with ground-based observations over the last 2 decades–an AeroCom and CMIP6 analysis, Atmos. Chem. Phys., 20, 13355-13378, https://doi.org/10.5194/acp-20-13355-2020, 2020.

Mukkavilli, S., Prasad, A., Taylor, R., Huang, J., Mitchell, R., Troccoli, A., and Kay, M.: Assessment of atmospheric aerosols from two reanalysis products over Australia, Atmos. Res., 215, 149-164, https://doi.org/10.1016/j.atmosres.2018.08.026, 2019.

Nagaraja Rao, C., Stowe, L., and McClain, E.: Remote sensing of aerosols over the oceans using AVHRR data Theory, practice and applications, Int. J. Remote Sens., 10, 743-749, https://doi.org/10.1080/01431168908903915, 1989.

Nakajima, T., Campanelli, M., Che, H., Estellés, V., Irie, H., Kim, S.-W., Kim, J., Liu, D., Nishizawa, T., and Pandithurai, G.: An overview of and issues with sky radiometer technology and SKYNET, Atmos. Meas. Tech., 13, 4195-4218, https://doi.org/10.5194/amt-13-4195-2020, 2020.

NOAA, DOD, FAA, and USN: Automated Surface Observing System (ASOS) User's Guide, 1998.

O'Reilly, J. E., Maritorena, S., Mitchell, B. G., Siegel, D. A., Carder, K. L., Garver, S. A., Kahru, M., and McClain, C.: Ocean color chlorophyll algorithms for SeaWiFS, J. Geophys. Res., 103, 24937-24953, https://doi.org/10.1029/98jc02160, 1998.

Pebesma, E. J.: Multivariable geostatistics in S: the gstat package, Comput. Geosci., 30, 683-691, https://doi.org/10.1016/j.cageo.2004.03.012, 2004.

Qiu, J. and Lin, Y.: A parameterization model of aerosol optical depths in China, Acta. Meteorol. Sin., 59, 368-372, https://doi.org/10.11676/qxxb2001.039, 2001.

Ramanathan, V., Crutzen, P. J., Kiehl, J., and Rosenfeld, D.: Aerosols, climate, and the hydrological cycle, Science, 294, 2119-2124, https://doi.org/10.1126/science.1064034, 2001.

Remer, L. A., Kleidman, R. G., Levy, R. C., Kaufman, Y. J., Tanre, D., Mattoo, S., Martins, J. V., Ichoku, C., Koren, I., Yu, H., and Holben, B. N.: Global aerosol climatology from the MODIS satellite sensors, J. Geophys. Res-Atmos., 113, https://doi.org/10.1029/2007jd009661, 2008.

Remer, L. A., Kaufman, Y. J., Tanre, D., Mattoo, S., Chu, D. A., Martins, J. V., Li, R. R., Ichoku, C., Levy, R. C., Kleidman, R. G., Eck, T. F., Vermote, E., and Holben, B. N.: The MODIS aerosol algorithm, products, and validation, J. Atmos. Sci., 62, 947-973, https://doi.org/10.1175/jas3385.1, 2005.

Salomonson, V. V., Barnes, W. L., Maymon, P. W., Montgomery, H. E., and Ostrow, H.: MODIS: advanced facility instrument for studies of the Earth as a system, Ieee T. Geosci. Remote., 27, 145-153, https://doi.org/10.1109/36.20292, 1987.

Sawamura, P., Vernier, J. P., Barnes, J. E., Berkoff, T. A., Welton, E. J., Alados-Arboledas, L., Navas-Guzmán, F., Pappalardo, G., Mona, L., and Madonna, F.: Stratospheric AOD after the 2011 eruption of Nabro volcano measured by lidars over the Northern Hemisphere, Environ. Res. Lett., 7, 34013-34021(34019), https://doi.org/10.1088/1748-9326/7/3/034013, 2012.

Schutgens, N., Tsyro, S., Gryspeerdt, E., Goto, D., Weigum, N., Schulz, M., and Stier, P.: On the spatio-temporal representativeness of observations, Atmos. Chem. Phys., 17, 9761-9780, https://doi.org/10.5194/acp-17-9761-2017, 2017.

Singh, A., Mahata, K. S., Rupakheti, M., Junkermann, W., Panday, A. K., and Lawrence, M. G.: An overview of airborne measurement in Nepal–Part 1: Vertical profile of aerosol size, number, spectral absorption, and meteorology, Atmos. Chem. Phys., 19, 245-258, https://doi.org/10.5194/acp-19-245-2019, 2019.

Smirnov, A., Holben, B., Slutsker, I., Giles, D., McClain, C., Eck, T., Sakerin, S., Macke, A., Croot, P., and Zibordi, G.: Maritime aerosol network as a component of aerosol robotic network, J. Geophys. Res-Atmos., 114, https://doi.org/10.1029/2008JD011257, 2009.

Steinberg, D. and Colla, P.: CART: classification and regression trees, The top ten algorithms in data mining, 9, 179, 2009.

Streets, D. G., Yan, F., Chin, M., Diehl, T., Mahowald, N., Schultz, M., Wild, M., Wu, Y., and Yu, C.: Anthropogenic and natural contributions to regional trends in aerosol optical depth, 1980–2006, J. Geophys. Res-Atmos., 114, https://doi.org/10.1029/2008JD011624, 2009.

Sun, E., Xu, X., Che, H., Tang, Z., Gui, K., An, L., Lu, C., and Shi, G.: Variation in MERRA-2 aerosol optical depth and absorption aerosol optical depth over China from 1980 to 2017, J. Atmos. Sol-Terr. Phy., 186, 8-19, https://doi.org/10.1016/j.jastp.2019.01.019, 2019.

Sun, Y. and Zhao, C.: Influence of Saharan dust on the large-scale meteorological environment for development of tropical cyclone over North Atlantic Ocean Basin, J. Geophys. Res-Atmos., 125, e2020JD033454, https://doi.org/10.1029/2020JD033454, 2020.

Teixeira, A.: Classification and regression tree, Rev. Mal. Respir., 21, 1174-1176, https://doi.org/10.1016/S0761-8425(04)71596-X, 2004.

Tian, X., Tang, C., Wu, X., Yang, J., Zhao, F., and Liu, D.: The global spatial-temporal distribution and EOF analysis of AOD based on MODIS data during 2003-2021, Atmos. Environ., 302,

https://doi.org/10.1016/j.atmosenv.2023.119722, 2023.

Tupper, A., Oswalt, J. S., and Rosenfeld, D.: Satellite and radar analysis of the volcanic‑cumulonimbi at Mount Pinatubo, Philippines, 1991, J. Geophys. Res-Atmos., 110, https://doi.org/10.1029/2004JD005499, 2005.

Vernier, J. P., Thomason, L. W., Pommereau, J. P., Bourassa, A., Pelon, J., Garnier, A., Hauchecorne, A., Blanot, L., Trepte, C., and Degenstein, D.: Major influence of tropical volcanic eruptions on the stratospheric aerosol layer during the last decade, Geophys. Res. Lett., 38, https://doi.org/10.1029/2011GL047563, 2011.

Wang, K., Dickinson, R. E., and Liang, S.: Clear Sky Visibility Has Decreased over Land Globally from 1973 to 2007, Science, 323, 1468-1470, https://doi.org/10.1126/science.1167549, 2009.

Wang, K. C., Dickinson, R. E., Su, L., and Trenberth, K. E.: Contrasting trends of mass and optical properties of aerosols over the Northern Hemisphere from 1992 to 2011, Atmos. Chem. Phys., 12, 9387-9398, https://doi.org/10.5194/acp-12-9387-2012, 2012.

Wei, J., Li, Z., Peng, Y., and Sun, L.: MODIS Collection 6.1 aerosol optical depth products over land and ocean: validation and comparison, Atmos. Environ., 201, 428-440, https://doi.org/10.1016/j.atmosenv.2018.12.004, 2019.

Wei, J., Li, Z., Sun, L., Peng, Y., Liu, L., He, L., Qin, W., and Cribb, M.: MODIS Collection 6.1 3 km resolution aerosol optical depth product: Global evaluation and uncertainty analysis, Atmos. Environ., 240, 117768, https://doi.org/10.1016/j.atmosenv.2020.117768, 2020.

Welton, E. J., Campbell, J. R., Berkoff, T. A., Spinhirne, J. D., and Starr, D. O.: The micro-pulse lidar network (MPLNET), Frontiers in Optics, https://doi.org/10.1364/fio.2003.mk2, 2002.

Winker, D. M., Tackett, J. L., Getzewich, B. J., Liu, Z., Vaughan, M. A., and Rogers, R. R.: The global 3-D distribution of tropospheric aerosols as characterized by CALIOP, Atmos. Chem. Phys., 13, 3345-3361, https://doi.org/10.5194/acp-13-3345-2013, 2013.

Winker, D. M., Vaughan, M. A., Omar, A., Hu, Y., Powell, K. A., Liu, Z., Hunt, W. H., and Young, S. A.: Overview of the CALIPSO Mission and CALIOP Data Processing Algorithms, J. Atmos. Ocean. Tech., 26, 2310-2323, https://doi.org/10.1175/2009jtecha1281.1, 2009.

Wu, J., Luo, J., Zhang, L., Xia, L., Zhao, D., and Tang, J.: Improvement of aerosol optical depth retrieval using visibility data in China during the past 50years, J. Geophys. Res-Atmos., 119, 13370-13387, https://doi.org/10.1002/2014jd021550, 2014.

Xia, X., Che, H., Zhu, J., Chen, H., Cong, Z., Deng, X., Fan, X., Fu, Y., Goloub, P., and Jiang, H.: Ground-based remote sensing of aerosol climatology in China: Aerosol optical properties, direct radiative effect and its parameterization, Atmos. Environ., 124, 243-251, https://doi.org/10.1016/j.atmosenv.2015.05.071, 2016.

Yang, X., Zhao, C., Yang, Y., and Fan, H.: Long-term multi-source data analysis about the characteristics of aerosol optical properties and types over Australia, Atmos. Chem. Phys., 21, 3803-3825, https://doi.org/10.5194/acp-21-3803-2021, 2021a.

Yang, X., Zhao, C., Yang, Y., Yan, X., and Fan, H.: Statistical aerosol properties associated with fire events from 2002 to 2019 and a case analysis in 2019 over Australia, Atmos. Chem. Phys., 21, 3833-3853, https://doi.org/10.5194/acp-21-3833-2021, 2021b.

Yang, X., Wang, Y., Zhao, C., Fan, H., Yang, Y., Chi, Y., Shen, L., and Yan, X.: Health risk and disease burden attributable to long-term global fine-mode particles, Chemosphere, 287, https://doi.org/10.1016/j.chemosphere.2021.132435, 2022.

Yang, Y., Ge, B., Chen, X., Yang, W., Wang, Z., Chen, H., Xu, D., Wang, J., Tan, Q., and Wang, Z.:

1383   Impact of water vapor content on visibility: Fog-haze conversion and its implications to pollution control,

1384   Atmos. Res., 256, https://doi.org/10.1016/j.atmosres.2021.105565, 2021c.

1385   Yoon, J., Burrows, J., Vountas, M. v., von Hoyningen-Huene, W., Chang, D., Richter, A., and Hilboll, A.:

1386   Changes in atmospheric aerosol loading retrieved from space-based measurements during the past decade,

1387   Atmos. Chem. Phys., 14, 6881-6902, https://doi.org/10.5194/acp-14-6881-2014, 2014.

1388   Yoon, J., Pozzer, A., Chang, D. Y., Lelieveld, J., Kim, J., Kim, M., Lee, Y., Koo, J.-H., Lee, J., and Moon,

1389   K.: Trend estimates of AERONET-observed and model-simulated AOTs between 1993 and 2013, Atmos.

1390   Environ., 125, 33-47, https://doi.org/10.1016/j.atmosenv.2015.10.058, 2016.

1391   Zhang, S., Wu, J., Fan, W., Yang, Q., and Zhao, D.: Review of aerosol optical depth retrieval using

1392   visibility data, Earth-Sci. Rev., 200, 102986, https://doi.org/10.1016/j.earscirev.2019.102986, 2020.

1393   Zhang, Z., Wu, W., Wei, J., Song, Y., Yan, X., Zhu, L., and Wang, Q.: Aerosol optical depth retrieval from

1394   visibility in China during 1973-2014, Atmos. Environ., 171, 38-48,

1395   https://doi.org/10.1016/j.atmosenv.2017.09.004, 2017.

1396   Zhao, A. D., Stevenson, D. S., and Bollasina, M. A.: The role of anthropogenic aerosols in future

1397   precipitation extremes over the Asian Monsoon Region, Clim. Dynam., 52, 6257-6278,

1398   https://doi.org/10.1007/s00382-018-4514-7, 2019.